東京大学 大学院新領域創成科学研究科
基盤科学研究系物質系専攻

平成 27 年度
修士論文

Experimental Study of Quantum Spin-Orbital Entangled Systems
量子スピン軌道相関系の実験的研究

２０１５年7月１４日提出
指導教員：中辻　知　准教授

47-136035：HALIM MARIO

Acknowledgment

I would like to express my deepest gratitude to my supervisor, Prof. Satoru Nakatsuji, who provides me with excellent guidance and useful discussion. Also, I would like to thank Prof. Agung Nugroho who introduced me to Nakatsuji laboratory for the first time and supporting me with his expertise in single crystal growth. My sincere gratitude also to Prof. Yoshitomo Karaki, who helped me a lot during low temperature measurement by dilution refrigerator. My thanks also to Prof. Hiroshi Sawa for his support in the crystal structure calculation and X-ray measurement.

I thank Dr. Kenta Kimura, my senior and co-worker on this project, whose diligence and brilliance has inspired me to work hard every day. My thanks also to Dr. Kentarou Kuga, who helped me with the low temperature specific heat measurement and analysis. I learnt a lot from both of them. Thank you also to Shintarou Suzuki, my classmate and lab mate, whom I work together with during measurement by the dilution refrigerator. And thank you to all members of Nakatsuji laboratory, who inspired me and cheered me every time.

My thanks also to the technicians in ISSP who helped me a lot in crystal growth and characterization. Thank you to Mr. Kitazawa for letting me used his furnace to grow my single crystal. Thank you also to Mr. Koike, who helped me with the chemical analysis by ICP measurement.

Last but not the least, I would like thank both my family and friends, who gave me tremendous moral support during my study in Japan.

Finally. this thesis would not have been possible without the financial support provided by .Japanese Government Scholarship. I am very grateful for the chance that was given to me to study in one of the best universities in Japan.

Kashiwa, 14 July 2015

Mario Halim

Table of Contents

Acknowledgment i

Table of Contents ii

Chapter 1. Introduction 1

1.1. Symmetry Breaking Order and Landau Order Parameter 1

1.2. Fractional Quantum Hall Effect and Topological Order 3

1.3. Geometrically Frustrated System 6

Chapter 2. Experimental Study on $Ba_3CuSb_2O_9$ 11

2.1. Crystal Structure 11

2.2. Magnetic Properties 12

2.3. Absence of Jahn-Teller Distortion in Hexagonal Samples 13

2.4. Spin-orbital Correlation in $Ba_3CuSb_2O_9$ 15

Chapter 3. Experimental Methods 17

3.1. Synthesis 17

3.1.1. Polycrystalline sample 17

3.1.2. Single crystalline sample 19

3.2. Characterization 20

3.2.1. X-ray Diffraction 20

3.2.2. Magnetization 22

3.2.3. Specific Heat 24

Chapter 4. Results and Discussion **29**

4.1. X-ray Diffraction 29

4.1.1. Polycrystalline sample 29

4.1.2. Single crystalline sample 30

4.2. Magnetic Susceptibility 31

4.2.1. DC Susceptibility 31

4.2.2. AC Susceptibility 34

4.3. Specific Heat 36

Chapter 5. Conclusion **40**

Chapter 1
Introduction

1.1. Symmetry Breaking Order and Landau Order Parameter

The study in condensed matter physics has always been concerned about the states of matter, and the change associated with their energy. Aside from the well known solid, liquid and gas states, there are many other states which have been discovered by scientists, for example: ferromagnet and antiferromagnet, superconductor, superfluid, liquid crystal, and so on. The numbers of newly discovered states keep increasing, thus a general framework to describe these states is required. Through a long process, we know that these states actually possess different symmetry. The symmetry of an object is defined by how many ways it can transform (e.g. rotated or translated) without changing its initial appearances. A sphere is rotationally invariant, meaning it can be rotated by any angle without changing its appearance. A cube, on the other hand, is not rotationally invariant. It only have limited amount of rotation axis about which it can rotate to give equal appearance. The cube, therefore, breaks the rotational symmetry of real space. Considering the symmetry in states of matter, the less ordered the states the higher the symmetry. Water for example, seems to be disordered in its liquid form, but actually has more symmetry compared to its solid form. One can rotates water structure by any angle and still obtains water structure by definition. On the other hand ice does not possess the same rotational symmetry. An ice structure is defined by certain periodic structure, which breaks both translational and rotational symmetry. Thus, these two states are different in symmetry and a phase transition from water to ice can be regarded as *symmetry breaking* process.

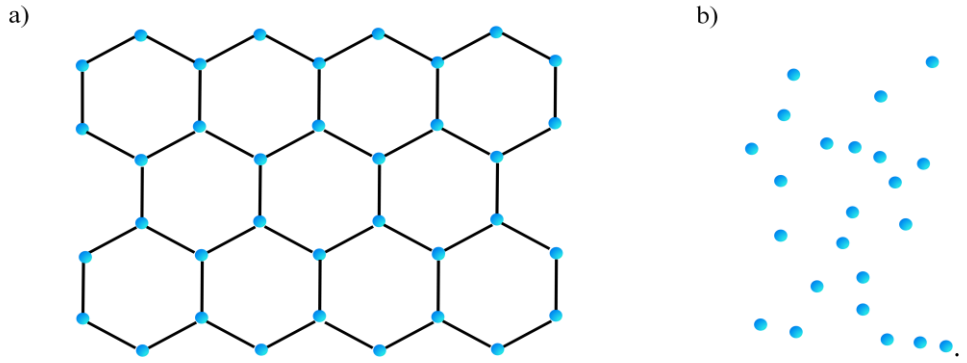

Figure 1.1 a) Ice structure viewed along *c*-axis. Hydrogen atoms are omitted for clarity. The oxygen atoms (blue) are arranged in hexagon lattice, which breaks translational symmetry (the pattern can be reproduced by placing oxygen atom at certain position relative to other oxygen atom) and rotational symmetry (one need to rotate by 60 degrees to obtain the same pattern). b) Water structure, on the other hand, does not have any specific pattern, so translational and rotational operations do not produce any significant difference.

The theory which relates phase transition and symmetry breaking was first developed by Landau[1] to explain second-order phase transition. In second-order phase transition, the system changes continuously from disordered, high temperature phases, to ordered states. The symmetry is continuously lowered below the transition temperature that the ground state symmetry possesses lower symmetry than its Hamiltonian. This phenomenon is known as *spontaneous symmetry breaking*, which leads to a number of equivalent ground states (with same symmetry) but macroscopically different and cannot be connected to each other by thermal fluctuation. An order parameter is then introduced to describe this broken symmetry. The order parameter value should be zero in disordered (symmetric) state and non-zero in ordered (non-symmetric) state. A simple example would be the Ising ferromagnet. In Ising ferromagnet model, spins can point to any of the two directions (e.g. either up or down). The symmetry of its Hamiltonian is invariant under spin inversion ($s_i \rightarrow -s_i$). However, the ground state below it Curie temperature is not invariant under such transformation. This illustrates the broken symmetry of the ground states. The good choice for order parameter here would be the magnetization $M = \mu S$ (i.e. a ferromagnet does not show spontaneous magnetization above its Curie temperature). A solid, as explained above, is also a symmetry broken state characterized by broken translational and rotational symmetry. The order parameter here would be average density wave. Landau's introduction of order parameter to explain ordered states has been very successful to explain and classify various symmetry broken states.

The key idea in Landau's theory is the assumption of free energy function as function of order parameters. In the vicinity of the symmetry breaking (second-order) phase transition, the order parameter function changes smoothly from zero to non-zero value and it is suggested that the behavior near transition point can be approximated by low-order polynomial function (Taylor expansion). In the case of second order phase transition with temperature as external parameter, the free energy F as function of order parameter G takes form as

$$F(G) = G_0 + \frac{1}{2}a(T - T_C)G^2 + \frac{1}{4}bG^4 \tag{1.1}$$

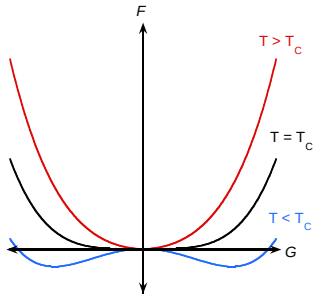

Figure 1.2 Free energy F, plotted as function of order parameter G for second-order phase transition. New minima at non-zero can be observed at temperature below critical temperature.

This free energy function is then minimized to obtain order parameter at an equilibrium state. Other properties such as entropy, specific heat, and the susceptibility can be obtained from this free energy expression. Landau's introduction of order parameter to explain ordered states has been very successful to predict the behavior of the most

systems near its transition point. However, it was later found that broken symmetry alone is not enough to identify certain type of are ordered state that cannot be characterized based on Landau's definition of order parameter.

1.2. Fractional Quantum Hall Effect and Topological Order

In 1982, scientists discover a new kind of state that cannot be explained by Landau's theory. In their experiment, they measured Hall conductance of certain semiconductor structure (GaAs-(Ga,Al)As heterojunctions) in high magnetic field at low temperature. Application of magnetic field would lead to the quantization of electron cyclotron orbital motion (Landau quantization), creating discrete energy level that can be accessed by increasing magnetic field. The system will oscillate between "insulating" and "conducting" state as Landau level is filled with electrons. When the Landau level is half filled, chemical potential μ lies in the Landau level and system behaves like a metal. On the other hand, when Landau level is completely filled with electron, chemical potential now lies on the gap between the Landau levels (here it is assumed that magnetic field is high enough so that the Landau levels are well-defined/ separated). Quantum Hall Effect used basically the same setup as the conventional Hall measurement, so the derivation for Hall resistance is quite similar. Here, the Hall conductance is defined as the tensor which relates current density J and electric field E in both x and y direction.

$$\begin{pmatrix} J_x \\ J_y \end{pmatrix} = \begin{pmatrix} \sigma_{xx} & \sigma_{xy} \\ -\sigma_{xy} & \sigma_{xx} \end{pmatrix} \begin{pmatrix} E_x \\ E_y \end{pmatrix} \tag{1.2}$$

The resistivity is then defined as

$$\begin{aligned} \rho_{xx} &\equiv \frac{E_x}{J_x} = \frac{\sigma_{xx}}{\sigma_{xx}^{\,2} + \sigma_{xy}^{\,2}} \\ \rho_{xy} &\equiv \frac{E_y}{J_x} = \frac{\sigma_{xy}}{\sigma_{xx}^{\,2} + \sigma_{xy}^{\,2}} \end{aligned} \tag{1.3}$$

Assuming no current flows in y-direction and magnetic field is high enough, $\omega_c\tau \gg 1$ and $\sigma_{xx} \gg \sigma_{yy}$, then the expression above can be approximated by

$$\begin{aligned} \rho_{xx} &\approx \frac{\sigma_{xx}}{\sigma_{xy}^{\,2}} \\ \rho_{xy} &\approx \frac{1}{\sigma_{xy}^{\,2}} \end{aligned} \tag{1.4}$$

Hall resistance R_H is defined as

$$R_H \equiv \frac{E_y}{J_x B} = \frac{V_y}{IB} = -\frac{1}{ne} \tag{1.5}$$

and Landau level filling factor ν can be defined as

$$\nu \equiv \frac{nh}{eB} = \frac{\sigma_H h}{e^2} \tag{1.6}$$

Here, e is elementary charge, h is Planck constant, n is number of electron per unit area, B is magnetic field strength, I and V are current and potential respectively. As mentioned above, the Hall resistivity will oscillate as magnetic field increase. In between "insulating" and "conducting" states is a plateau region where Hall resistivity σ_{xy} is constant. Each of these plateaus corresponds to quantum Hall states. The filling factors which correspond to the density of these states are multiplication of certain rational number (e.g. 1, 1/3, 2/5, 4/9, etc). The integer filling factor corresponds to integral Quantum Hall states while non-integer ν corresponds to fractional Quantum Hall states. Integral Quantum Hall states can be understood in terms of Landau level splitting described above. However, the fractional Quantum Hall states required more non-trivial approach. Nevertheless, the existence of certain filling factor suggests that there is some sort of order, which cannot be described by symmetry theory (they are different states, however without apparent symmetry difference). Later, it was realized that such kind of order belong to a new type of order, called *topological* order.

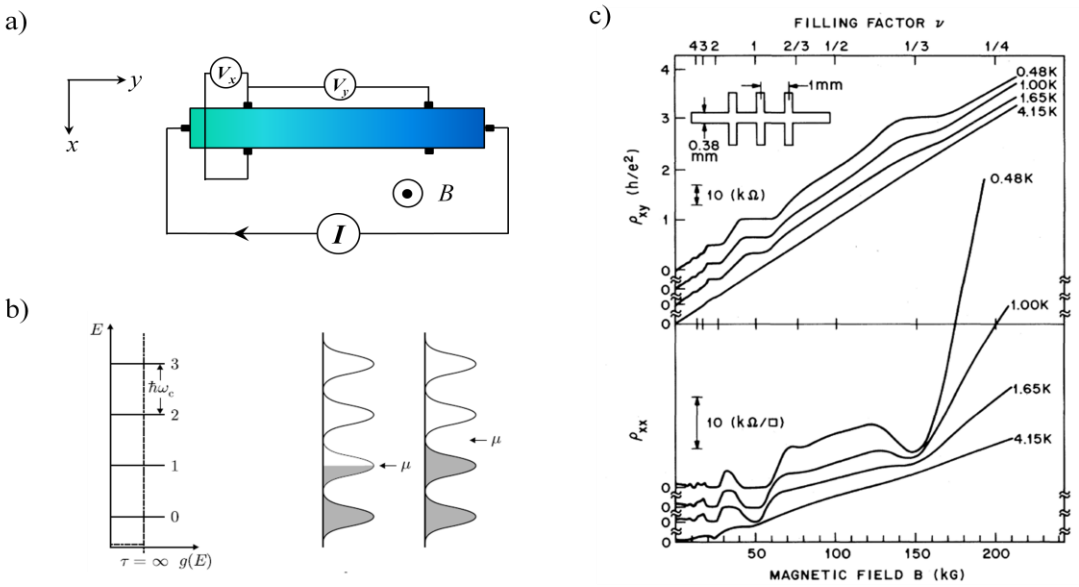

Figure 1.3 a) Schematic of typical Hall measurement and b) Landau level splitting under magnetic field. Right figure indicate two possible cases: "conducting" and "insulating" states c) Fractional Quantum Hall states observed in GaAs-$Al_{0.3}$-$Ga_{0.7}$As heterojunctions[2].

To understand the concept of topology, one can think of transforming an object into another by 'stretching', without 'cutting' any part. If two objects belong to the same topology class, it can be reversibly transform into one another by 'stretching' it. A popular analogy would be the topology between a donut and a cup of coffee. Practically, if one keeps stretching a donut, it can transform *continuously* into a coffee cup. So, we can say that they belong to the same topology class. On the other hand, a knot cannot be transformed into loop without cutting one part.

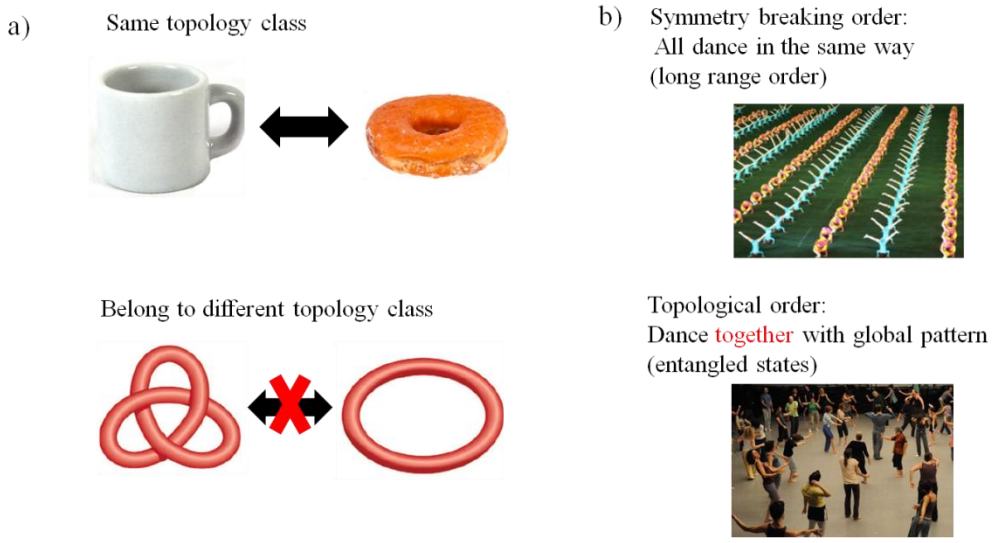

Figure 1.4 Illustration of the concept of topology. Two objects belong to the same topology if it can continuously transform into another object (i.e. just by 'stretching' it). b) The differences between symmetry breaking order such as antiferromagnet to the topological order such as Fractional Quantum Hall states by taking 'dancing pattern' as the intuitive picture [3].

The topological order is basically our classification for a certain type of order (that is rather subtle) which belongs to the same class of a certain 'topology'. While the complete picture of topological order remains unknown, there are several signs that indicate the presence of topological order. One is the absence of spontaneous symmetry breaking and the other being the existence of long-range quantum entanglement. Topological order presents us a new paradigm in condensed matter. It is a phenomenon that extends to various quantum systems, from high T_C superconductors to quantum spin liquid. The topological properties imply that the ground state degeneracy of these phases is only determined by its topology. Moreover, the topological order offers us the possibility of finding new kind of particle, namely the fractional quasiparticles (such as in fractional quantum Hall effect) that obey fractional statistics, and a new, collective excitations above the ground state (analog to a spin wave excitation in a magnetic order).

1.3. Geometrically Frustrated System

The Fractional Quantum Hall effect is just an example of novel properties in quantum phases. In most materials, such quantum phase cannot always be found, particularly because the symmetry breaking occurs at a high temperature. However, by introducing frustration into the system one can suppress this symmetry breaking order to much lower temperature, where quantum fluctuations are more dominant.

To understand the concept of frustration, one can consider magnetic spins placed on the corners of a triangle that are coupled antiferromagnetically with each other. Here, we would like to find the minimum energy of the system (ground state) by pairing the spins with opposite direction. When the spin direction is constrained along one axis (e.g. up or down), it becomes clear that it is not possible to satisfy pairing rule for all spins simultaneously. Instead of having a single solution, we obtain several possible configurations which give the same energy. The ground state is said to be degenerate. The degeneracy in the ground state is one of the signatures of a frustrated system and this degeneracy eventually becomes macroscopic as the system size increases. Due to the geometry origin of such frustration, it is then called geometrical frustration.

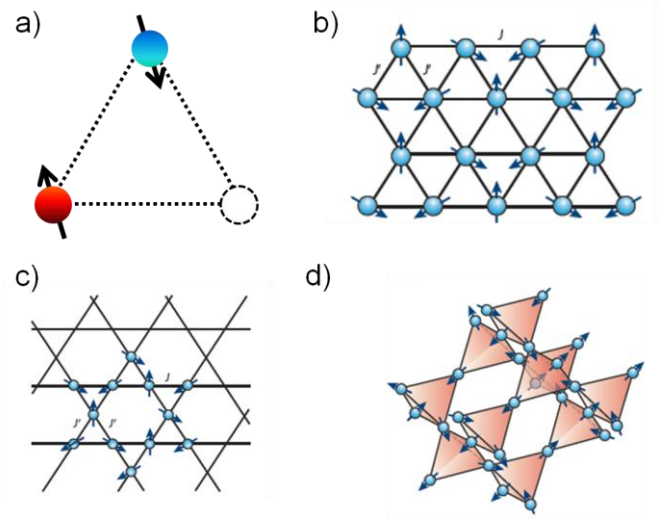

Figure 1.5 a) Geometrical frustration of Ising triangular antiferromagnet. Some examples of frustrated lattice[4]: In two-dimensional space; b) Triangular lattice, c) Kagome lattice; and in three-dimensional space; d) Pyrochlore lattice. Arrows indicate spin direction. In triangular and Kagome lattice, the rotational symmetry may not be perfect and exchange interaction J will become anisotropic (J and J').

The firstly investigated frustrated system is actually water ice. In 1945, motivated by the presence of residual entropy in water ice at low temperature, Pauling tried to model the water ice structure[5]. In his approach, each water molecule consists of tetrahedrally-coordinated oxygen ions, with each oxygen ion surrounded by two nearby, covalently bonded proton, and two further, hydrogen bond bonded protons (Figure 1.6 a). This structure is degenerate because each proton can select "near" or "far" position with respect to an oxygen ion while maintaining

the same configuration energy. Because there are 2 protons for each oxygen atom, there are 2^{2N} proton configurations for N oxygen atoms. For each oxygen ion, there are 16 configurations, but only six of them are energetically allowed after applying "ice rule" of 2-near, 2-far. This leads to the total number of configuration $W = (2)^{2N} (6/16)^N = (3/2)^N$ and the entropy is estimated to be $S_0 / k_B = ln\ 3/2 = 0.81$ cal/mol.K. This value is close to the experimentally obtained residual entropy of 0.82 cal/mol.K[7]. The large macroscopic degeneracy in water ice is only one of the examples, how cooperative phenomenon can be reflected as measurable quantities. In magnetic systems these cooperative phenomena are mainly acted on the electron spins. As the temperature is lowered, the thermal fluctuation of spins becomes smaller and quantum fluctuation dominates. However, the lower temperature also means lower energy, and sometimes the spins fall out of equilibrium into a symmetry broken state (in this case, magnetic order). Magnetic frustration serves to counter this ordered state by adding degeneracy to the ground state which suppresses the magnetic order to lower temperature.

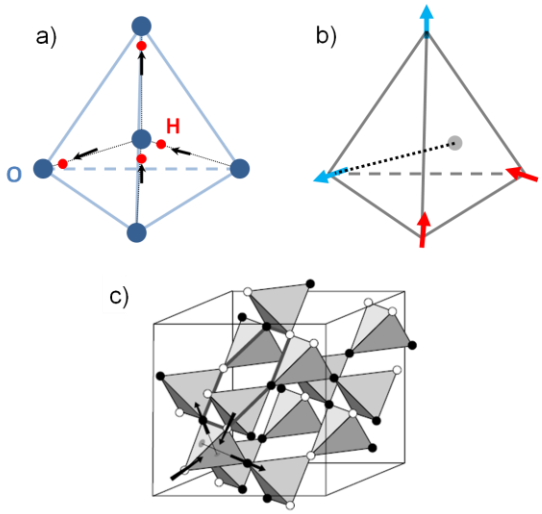

Figure 1.6 a) Two-near, two-far state in water ice. Arrows indicate the displacement vectors of protons from the midpoint of oxygen-oxygen bond. b) 2-in. 2-out state. Dotted lines indicate local <111> axis. c) 2-in, 2-out state on a pyrochlore lattice[6]. Black circles indicate spins that point outside and white circles indicate spins that point inside.

The physical realization of water ice model for magnetic system was first found in pyrochlore compound $Ho_2Ti_2O_7$[8]. In this compound, Ho^{3+} and Ti^{4+} ions form separate pyrochlore lattices (corner sharing tetrahedra). The magnetic properties of this compound are brought by the Ho^{3+} ions, which are located on the corner of each tetrahedron. Although no geometrical frustration is expected for ferromagnet in pyrochlore structure, it seems possible to have one when ferromagnetic coupling exist together with single-ion anisotropy. In $Ho_2Ti_2O_7$, the magnetic moment is large (~10μ_B) and the ground state is a doublet with Ising anisotropy along local <111> direction. This would result in spins pointing either towards or away from the body center of tetrahedron (Figure 1.6 b). The ground state of this material then can be realized by having two spins pointing in and out on each tetrahedron, a "two-in, two-out" state. Due to its similarities with the water ice, the model is named as spin ice.

Due to the large moment size, the firstly discovered rare-earth spin ice family can be regarded as *classical* spin ice, because of large energy required to tunnel between degenerate ground state. In classical spin ice, the spin eventually froze out into disordered state below certain temperature because the system no longer able to tunnel between the ground states. When the moment size is reduced, quantum fluctuation increases and it is proposed that such fluctuation of Heisenberg type spins on pyrochlore lattice would lead to a *quantum spin liquid* state, a correlated paramagnet without magnetic order down to very low temperature.

In 1973, P.W. Anderson proposed an alternative ground state for 2-D triangular lattice, which has lower energy compared to previously known Néel (i.e. antiferromagnetic) state[9]. The model, which is named as *Resonating Valence Bond* (RVB), has attracted interest, particularly due to its relation with the high temperature superconductivity phenomenon[10]. The Néel state for Heisenberg spin with nearest neighbor exchange on triangular lattice can be constructed by having spins on three sub-lattices pointed at 120° to each other. In RVB model, the spin forms valence bond pair (singlet) with nearby spin. When the anisotropy is minimal, all bonding directions have equal probability, and the spins can pair with any nearby spins. The ground state wave function then is a superposition of all possible valence bond configurations. The valence bond can be formed in short range or over the long range. The short range valence bond has energy gap, meaning that it cost finite energy to excite the spins. On the other hand, if the valence bond pairs the spins that are far apart, the bond strength is relatively weak and the excited state cost relatively much smaller energy. So, in long range RVB there will be large low energy density of states and it is possible to have *gapless* spectrum.

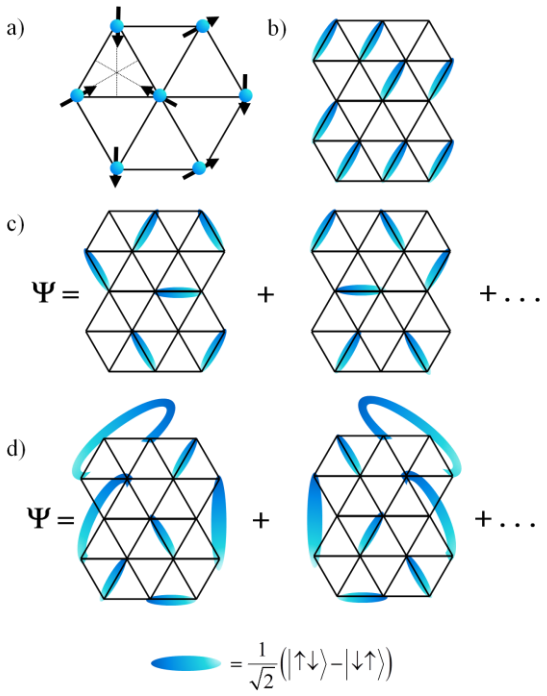

Figure 1.7 a) Néel 120° state on triangular lattice. b) Valence Bond Solid state. c) The short range RVB state. d) Long range RVB state

The anisotropic environment of the lattice may favor certain pairing direction over the other. The valence bond states formed on top of such lattice will have their symmetry broken. Hence, the resulting state is similar to valence bond crystal, a state which is called *Valence Bond Solid* (VBS) state.

The RVB state provides a primary description of a *spin liquid* state with its *unbroken symmetry* and its *liquid-like wave function*. It would be interesting to identify various spin liquid states and classify them. However, it is proven to be a challenging task due to the sheer number of possible spin liquid states. For example, X.G. Wen has discovered hundred types of quantum spin liquid states based on their symmetry for $S = 1/2$ antiferromagnet on square lattice[11].

The excitation in RVB states and spin liquid is *spinon*, a quasiparticle carrying zero net charge and spin half ($q = 0$, $S = 1/2$). In one dimensional antiferromagnet, a spinon is created by flipping series of spins from its antiferromagnet ground state. This will create domain walls between some spins (some adjacent spins will have the same orientation). If the amount flipped spins is finite one can see that spinons exist as a pair that may move freely within the chain (Figure 6a). On the triangular RVB state, the spinons basically are the unpaired spin, which can move by rearrangements of valence bonds (Figure 1.8 b)

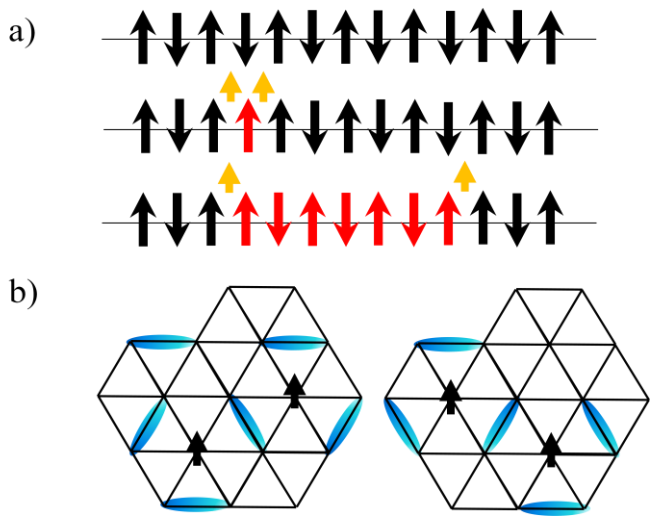

Figure 1.8 a) Spinon (yellow arrow) as domain wall in one-dimensional antiferromagnet chain. A pair of spinons can move within chain as more spins is flipped. b) Spinon (black arrow) in RVB state is unpaired spin which can move by rearranging valence bonds.

Now that we understand a bit about "what is spin liquid ground state", the next important question is "where to find it in real material" and "how to check whether it is a spin liquid or not". As we have discussed above, frustration and quantum fluctuation are both important in stabilizing disordered magnetic state at low temperature.

So, one should look into material which has frustrated lattice like, triangular, kagome, or pyrochlore lattice. Table 1.1 lists current candidates for Quantum Spin Liquid.

Compound	Lattice	θ_{CW} (K)	Frustration parameter f	Wilson ratio R	γ (mJ. $mol^{-1}.K^{-1}$)
κ -(BEDT-TTF)$_2$Cu$_2$(CN)$_3$	Triangular	-375	> 1000	1.8	19
EtMe$_3$Sb[Pd(dmit)$_2$]$_2$	Triangular	-350	> 1000	1.09	19.9
ZnCu$_3$(OH)$_6$Cl$_2$ (*herbersmithite*)	Kagome	-241	>1000	-	240
BaCu$_3$V$_2$O$_8$ (OH)$_2$ (*vesignieite*)	Kagome	-77	>100	4	50
Na$_4$Ir$_3$O$_8$	Hyperkagome	-650	>1000	70	1

Table 1.1 Several Quantum Spin Liquid candidates.

References:

1. Landau, L., Lifshitz, E.M. *Statistical Physics*. Pergamon Press: New York, NY,USA, 1980
2. Tsui, D. C. and Stormer, H. L. and Gossard, A. C.. *Phys.Rev.Lett.* **48** 1559 (1982)
3. Wen, X.G arXiv:1210.1281v2
4. Balents, L., *Nature* **464,** 199-208 (2010)
5. Pauling, L. *J.Am.Chem.Soc.* **57**, 2680 (1935)
6. Bramwell S.T. and M.J.P. Gingras, *Science* **294**, 1495-1500 (2001)
7. Gordon, A.R. *J.Chem.Phys.* **2**, 65 (1934)
8. Harris et al.,*Phys. Rev. Lett* **79**, 2554-2557 (1997)
9. Anderson, P.W. *Mater.Res.Bull.* **8**, 153-160 (1973)
10. Anderson, P.W., *Science* **235**, 1196-1198 (1987)
11. Wen, X.G., *Phys. Rev. B* **65**, 165113 (2002).

Chapter 2

Experimental Study on $Ba_3CuSb_2O_9$

2.1. Crystal Structure

$Ba_3CuSb_2O_9$ is initially reported in 1978 as a perovskite compound with layered triangular structure (space group : $P6_3mc$)[1]. A perovskite-type compound generally has a chemical formula of ABX_3 and it usually has BX_6 octahedra which can be linked by either face-sharing or corner-sharing joint, depends on the A site ion's size. If we are to rewrite $Ba_3CuSb_2O_9$ formula as $Ba(Cu_{1/3}Sb_{2/3})O_3$, the A-site will be occupied by barium and B-site will be shared by copper and antimony. This means there are both face-sharing $CuSbO_9$ bi-octahedra ("dumbbell") and corner-sharing SbO_6 octahedra. In this structure Cu ions form two-dimensional triangular lattice with its neighboring Cu, so in this structure a frustrated ground state is expected if the nearest-neighbor coupling is antiferromagnetic. In this structure Cu-Sb dumbbell in this structure possess three-fold rotational symmetry, which guarantees the orbital degeneracy of e_g orbital.

The X-ray experiments on single crystalline sample provide a new evidence on $Ba_3CuSb_2O_9$ actual space group. The space group is chosen based on the powder X-ray diffraction data by applying extinction rules on the reflection intensity. The extinction rule will limit the choice based on the translational, glide and screw symmetry, and the Bravais lattice, such as BCC, FCC, etc. However, extinction rule alone is not enough to determine centrosymmetry, existence of a mirror plane, rotational symmetry, etc. Thus, one needs to select the best space group by comparing calculated crystal structure factor, based on a structure model, with the experimental data.

First, from the synchrotron radiation single crystal X-ray diffraction, performed at the BL-02, SPring-8, the crystal system is determined as hexagonal with Laue group of 6/*mmm*. The extinction rule occurs when *l* is odd in the index family of *hhl*. This condition will narrow down the candidate space symmetry to either $P6_3mc$, $P\bar{6}2c$, or $P6_3/mmc$. Among these three space group, $P\bar{6}2c$ cannot describe the experimental observation, leaving two possible choices: $P6_3mc$ or $P6_3/mmc$. The non-centrosymmetric space group of $P6_3mc$ was chosen in the previous report [2].

However, the crystal structure factor calculation has indicated that centrosymmetric space group $P6_3/mmc$ is better in reproducing diffraction intensity, such as the intensity of *002* peak.

In the new space group $P6_3/mmc$, a mirror plane exists on the oxygen plane between two $CuSb_2O_9$ octahedra. Therefore, copper and antimony sites here are crystallographically equivalent. This choice is used to derive a honeycomb structure, by flipping one-third of Cu-Sb dumbbells. Now, some of the copper ions will occupy the sites which are originally occupied by the antimony ions. This alternative site of copper ion is labeled as Cu' sites.

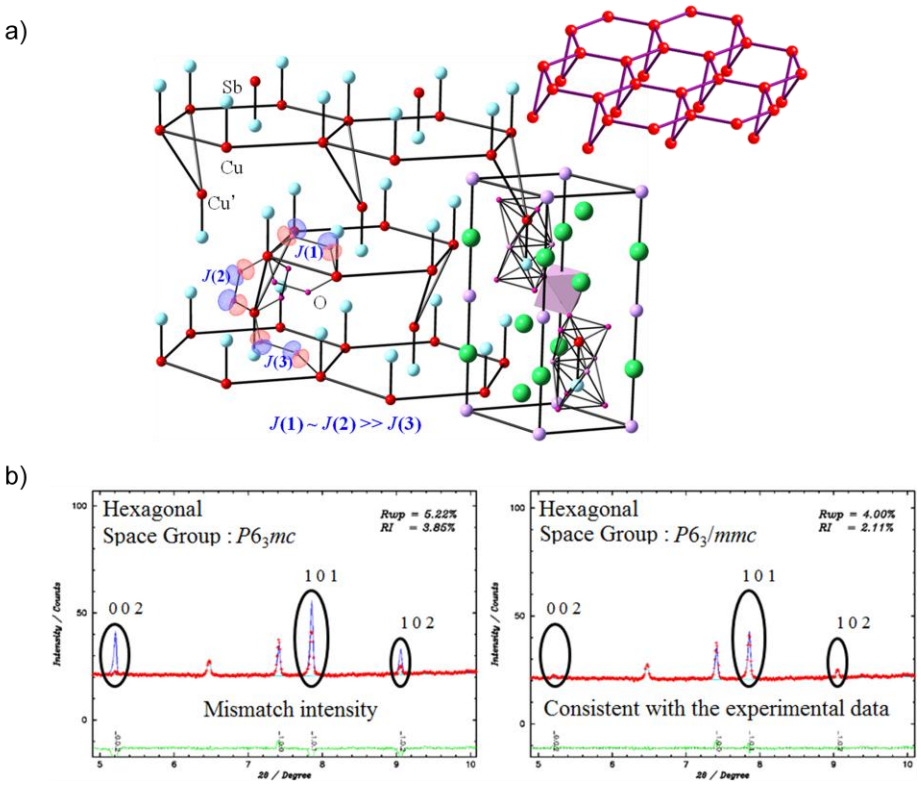

Figure 2.1 a) Honeycomb structure of $Ba_3CuSb_2O_9$, derived from new space group $P6_3/mmc$ [3]. b) Comparison between calculated and observed diffraction intensity for both space groups[5].

2.2. Magnetic properties

$Ba_3CuSb_2O_9$ has a frustrated ground state, as indicated by the absence of magnetic ordering down to 20 mK [3]. The high temperature susceptibility follows Curie-Weiss law (θ_{CW} ~50 K), while a deviation from Curie-Weiss behavior is observed in low temperature part. This deviation is commonly found in the system which has defect-like spins (orphan spins) [4]. In $Ba_3CuSb_2O_9$, such orphan spins may originate from copper ions in Cu' site.

The neutron scattering experiments performed at National Institute of Standards and Technology has indicated energy gap associated with spin singlet formation at T~ 50 K. Thus, the susceptibility should go to zero when all copper spins are paired. However, the magnetic susceptibility of $Ba_3CuSb_2O_9$ continuously increases at temperature decreases. This indicates that some parts of copper spins remain unpaired at low temperature. Therefore, the magnetic susceptibility of $Ba_3CuSb_2O_9$ can be thought as a sum of bulk and orphan spin susceptibility.

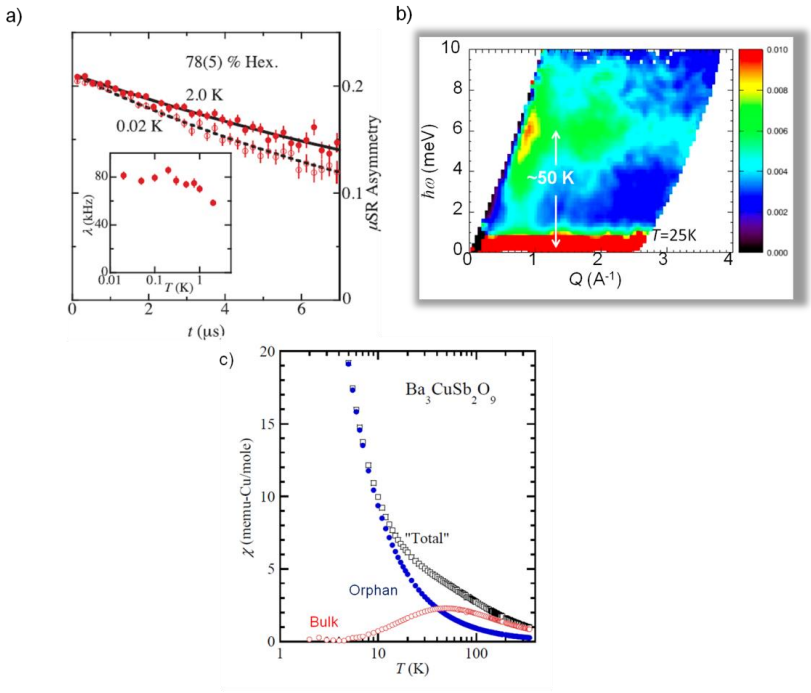

Figure 2.2 a) The absence of magnetic order as confirmed by μSR experiment. b) Energy gap of ~ 50 K observed in inelastic neutron scattering experiment. c) Total magnetic susceptibility as a sum of bulk and orphan spin susceptibility[3].

2.3. Absence of static Jahn-Teller distortion in hexagonal sample

In section 2.1, the correct space group for $Ba_3CuSb_2O_9$ has been determined to be $P6_3/mmc$. Although different from the previous report, this space group possesses Cu^{2+} orbital degrees of freedom provided by the three-fold symmetry axis on Cu-Sb dumbbell. Materials which have orbital degrees of freedom are known to undergo crystal distortion (Jahn-Teller distortion) at low temperatures. To confirm the existence of lattice distortion due to the Jahn-Teller effect in the $Ba_3CuSb_2O_9$, temperature dependence of the powder X-ray diffraction patterns for two different types of sample is investigated. At temperature below 200 K, the system exhibits a structural phase transition that lowers the structural symmetry. Based on the powder XRD structure analysis, we found that the space group is $P6_3/mmc$ at 300 K, but about 94% of the sample undergoes the structural phase transition into the low temperature, orthorhombic, *Cmcm* phase. When the hexagonal structure becomes distorted into the orthorhombic structure at low temperatures, the three-fold rotational symmetry of the dumbbell is lost, lifting the orbital degeneracy. Therefore, the observed orthorhombic distortion should be considered as the result of the cooperative JT effect.

The absence of static Jahn-Teller distortion in hexagonal sample is further confirmed by Electron Spin Resonance (ESR) study. ESR measurement is known to be useful in detecting anisotropy in crystal. The ESR measurements on hexagonal sample showed a clear single field-derivative Lorentzian-type signal down to 30 K, while clear splitting was observed for the orthorhombic sample. The angular-dependence of the g-factor along the *c*-

plane also shows no angular dependence in the hexagonal sample, while there are three periodic components correspond to the three-domain formed by the static Jahn-Teller distortion in the orthorhombic sample. Another ESR study has indicates a possibly dynamical Jahn-Teller distortion based on the frequency dependence of ESR signal in $Ba_3CuSb_2O_9$[7].

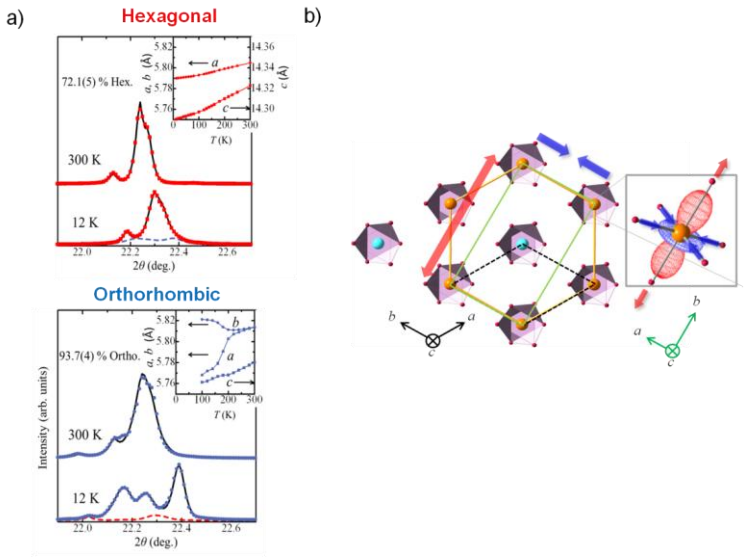

Figure 2.3 a) Hexagonal and orthorhombic sample powder diffraction at room and low temperature[3]. b) Hexagonal to orthorhombic structural transition[5].

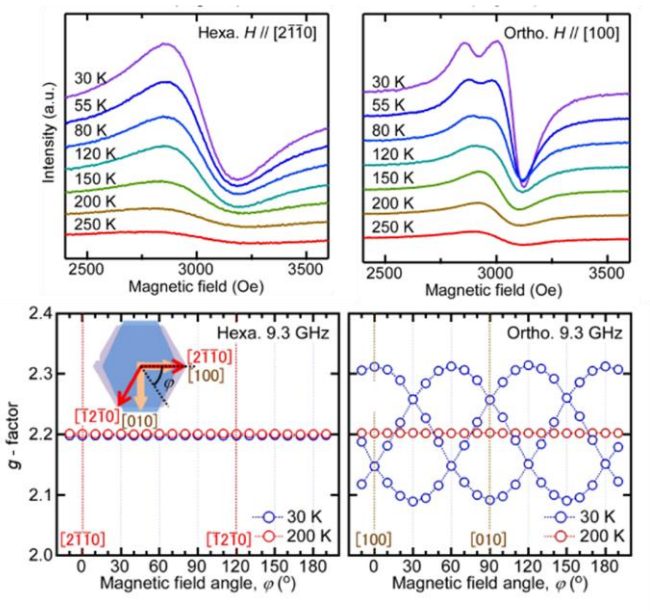

Figure 2.4 ESR measurements on hexagonal and orthorhombic sample[6].

2.4. Spin-Orbital Correlation in $Ba_3CuSb_2O_9$

The orbital and spin in $Ba_3CuSb_2O_9$ remain in disorder at low temperature. The next question would be " Is there any correlation between spin and orbital degrees of freedom?". An X-ray scattering study has indicate the possibility of spin orbital correlation in this system. This study investigates the diffuse scattering observed at particular Bragg point that caused by the Jahn-Teller distortion. The result indicates that spin and orbital are correlated down to low temperature.

Recent theoretical studies on honeycomb lattice have also pointed out the possibility of RVB state in this system [9]. Their model, which based on quantum dimer model on honeycomb lattice, has predicted a JT liquid state where both spin-orbital singlet and JT singlet coexist, creating a unique ground state for $Ba_3CuSb_2O_9$. In their spin-orbital resonant state proposed earlier, spin-orbital singlet is formed by σ bonding of d (x^2-y^2) orbitals. This singlet state will resonate to each other, due to the orbital degrees of freedom in Cu-Sb dumbbells.

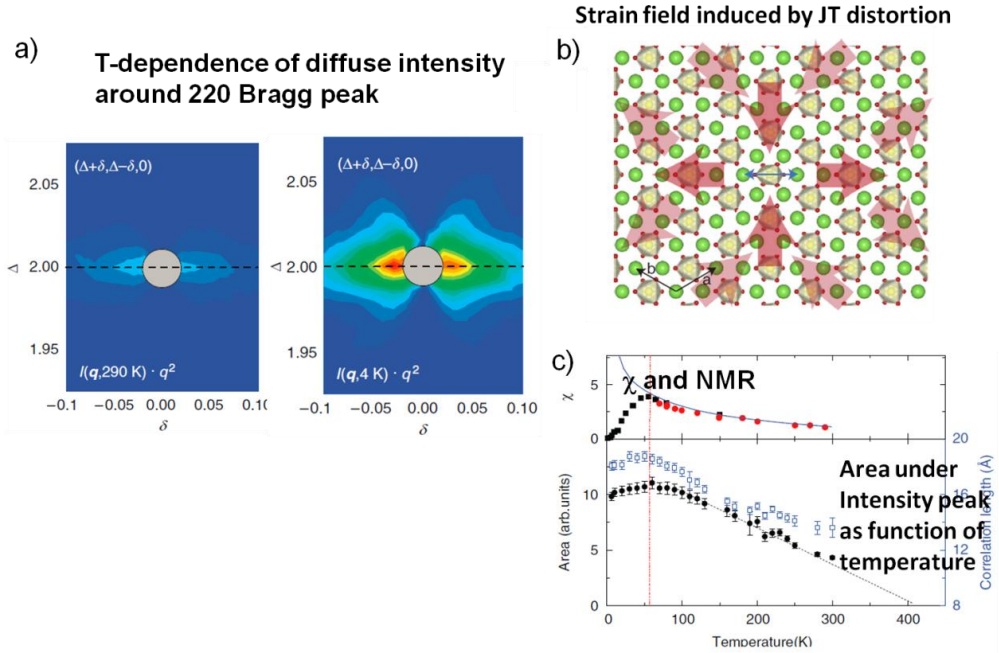

Figure 2.5 X-ray scattering study on $Ba_3CuSb_2O_9$ single crystal. a) Diffuse scattering at low temperature that is associated with JT distortion. b) Strain field profile that originates from JT distortion. c) Intensity under scanned area (dashed line in fig. 2.5.a) as function of temperature. A maximum which coincides with spin singlet formation temperature indicate possibility of spin-orbital correlation[8].

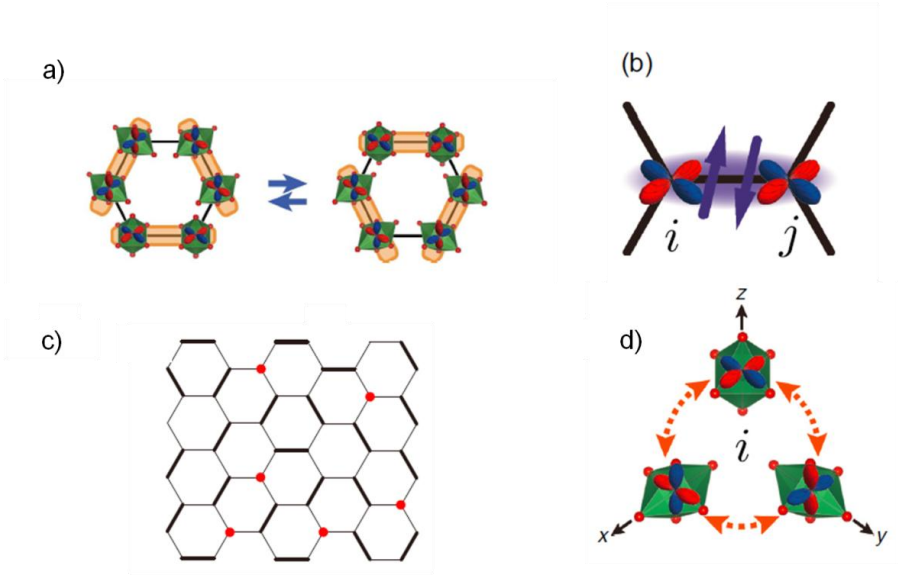

Figure 2.6 a) Spin-orbital Resonant State. b) Spin-orbital singlet dimer. c) Jahn-Teller liquid state. Bold lines indicate spin-orbital dimer and red dots indicate JT singlet. d) Jahn-Teller singlet [9, 10].

References:

1. Von. P. Köhl, *Z. Anorg. Allg. Chem.* **442**, 280 (1978)
2. H. D. Zhou et al., *Phys. Rev. Lett.* **106**, 147204 (2011)
3. S. Nakatsuji, et al., *Science* **336**, 559-563 (2012)
4. P. Schiffer and I. Daruka , *Phys. Rev. B* **56**, 21 (1997)
5. M. Halim, H. Sawa. S. Nakatsuji, *preprint* (2015)
6. N. Katayama, et al., *Proc. Natl. Acad. Sci. U.S.A. DOI: 10.1073/pnas.1508941112* (2015)
7. Y.Han et al., *preprint* (2015)
8. Y. Ishiguro et al., *Nature Communication* **4**, 2022 (2013)
9. J.Nasu and S.Ishihara, *Phys.Rev.B* **91**, 045117 (2015)
10. J. Nasu and S. Ishihara, *Phys. Rev. B* **90**, 179903 (2014)

Chapter 3
Experimental Method

3.1. Synthesis

3.1.1. Polycrystalline sample

Polycrystalline samples of $Ba_3CuSb_2O_9$ are prepared by a solid-state reaction method. A mixture of $BaCO_3$ (99.99%, *Rare Metallic*), CuO (99.9%, *High Purity Chemical*) and Sb_2O_3 (99.999%, *Rare Metallic*) are thoroughly mixed in an agate mortar, put into an alumina crucible, and calcined under air atmosphere at temperature of 900 °C for 12 hours, using a muffle furnace. The sample is then cooled normally to room temperature. The obtained powder is grounded and pressed into a pellet, and heated at 1100 °C for 20 hours under the same condition as described in the previous step.

The obtained pellet is then grounded into fine powder and checked for impurity phase by powder X-ray diffraction. The last heating procedure is repeated as necessary until single phase sample is obtained. Besides the procedure described above, there are also another way to obtain single phase of $Ba_3CuSb_2O_9$. At first, the single phase $Ba_3CuSb_2O_9$ was obtained by Method #1 (figure 3.1 a). In this method, the sample is repeatedly annealed with intermediary grinding in between. This method is quite successful in obtaining high quality polycrystalline sample as confirmed by the XRD and composition analysis. However, this method is the most time consuming, with total annealing time of nearly 100 hours.

Method #2 (figure 3.1 b) was then developed in order to reduce the time required to purify polycrystalline sample of $Ba_3CuSb_2O_9$. In method 2, an extra amount of antimony oxide (1.5%) is added into the starting material in order to compensate the loss due to the volatilization of Sb_2O_3 at high temperature. This method is successfully reduce total annealing time by half. However, by this method there is possibility of impurity phase formation ($BaSb_2O_6$) of which the main peaks overlap with $Ba_3CuSb_2O_9$ diffraction peaks.

Finally, in Method #3, the starting mixture is calcined (i.e. removal of carbon) at intermediate temperature before pressed and annealed at higher temperature. This method useful to improve homogeneity of sample after the first reaction as well as reducing total annealing time further to 32 hours.

Based on the quality of the final polycrystalline sample, characterized by XRD and ICP composition analysis, the best method would be the method #1. However, the resulting polycrystalline sample from these three methods is not significantly different. Therefore method #3 would be the best way in terms of efficiency to produce the polycrystalline sample of $Ba_3CuSb_2O_9$.

a) Method 1.
Repeated heating and intermediary grinding
Total sintering time : 112 h
# of intermediary grinding : 5 times

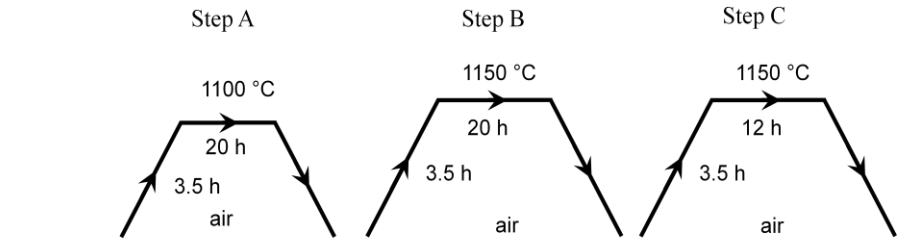

- Starting materials:
  3 $BaCO_3$ + **1** CuO + **1** Sb_2O_3
- Mixed & pressed into pellet
- Put into alumina crucible and heated inside muffle furnace

- Repeat step B three more times
- Intermediary grinding after each step
- Mixed, pressed into pellet and heated inside alumina crucible

b) Method 2.
Add extra Sb_2O_3 in starting material
Total sintering time : 50 h
# of intermediary grinding : 2 times

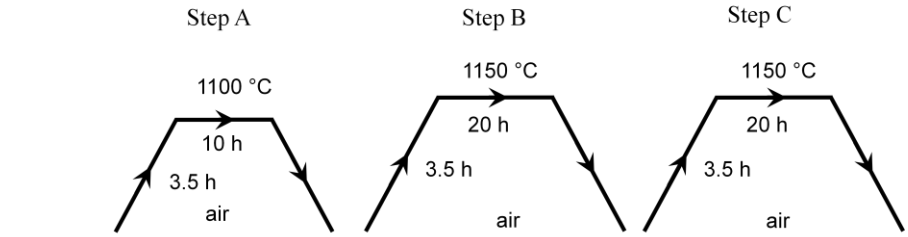

- Starting materials:
  3 $BaCO_3$ + **1** CuO + **1.015** Sb_2O_3
- Mixed & pressed into pellet
- Put into alumina crucible and heated inside muffle furnace

- Intermediary grinding after each step
- Mixed, pressed into pellet and heated inside alumina crucible

c) Method 3.
Calcination at lower temperature
Total sintering time : 32 h
# of intermediary grinding : 1 times

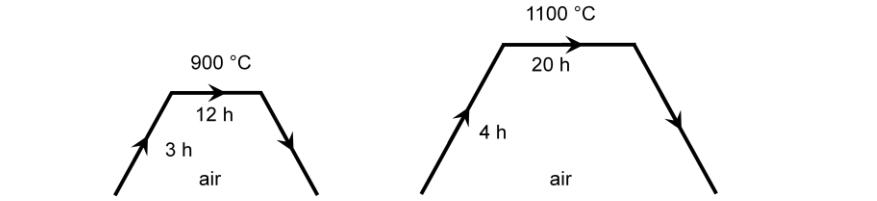

- Starting materials:
  3 $BaCO_3$ + CuO + Sb_2O_3
- Mixed and put into alumina crucible

- Intermediary grinding
- Press into pellet
- Put into alumina crucible

- Powder X-ray diffraction

Figure 3.1 Synthesis methods for polycrystalline sample of $Ba_3CuSb_2O_9$

3.1.2. Single crystalline sample

Single crystals of $Ba_3CuSb_2O_9$ are made by a flux method, using $BaCl_2$ as the flux. The polycrystalline sample and the flux ($BaCl_2$, 99.9%, *High Purity Chemical)* are put into a platinum crucible. A small amount (9 mol%) of $Ba(OH)_2$ is added into the flux. The addition of $Ba(OH)_2$ into the flux is necessary in order to obtain a hexagonal sample. The $Ba(OH)_2$ used in this experiment is obtained by heating appropriate amount of $Ba(OH)_2 .8H_2O$ in platinum crucible under argon gas flow at 100 °C for ~ 20 hours. The platinum crucible which contains polycrystalline sample and flux is tightly capped with a platinum lid and put inside alumina crucible. This alumina crucible is then suspended inside vertical furnace (Bridgman furnace) by an alumina rod and a platinum wire. The sample is then heated at 1140 °C for 12 hours and cooled slowly at a rate of 2 °C/hour to the temperature of 800 °C. During the synthesis, a *wet* oxygen gas (oxygen flow that passed through water) is flowed at a rate of 20 cc/min. After that, the sample is cooled normally to the room temperature.

The obtained product is washed with hot water to remove the remaining flux. Finally, the sample is washed with acetone and dried.

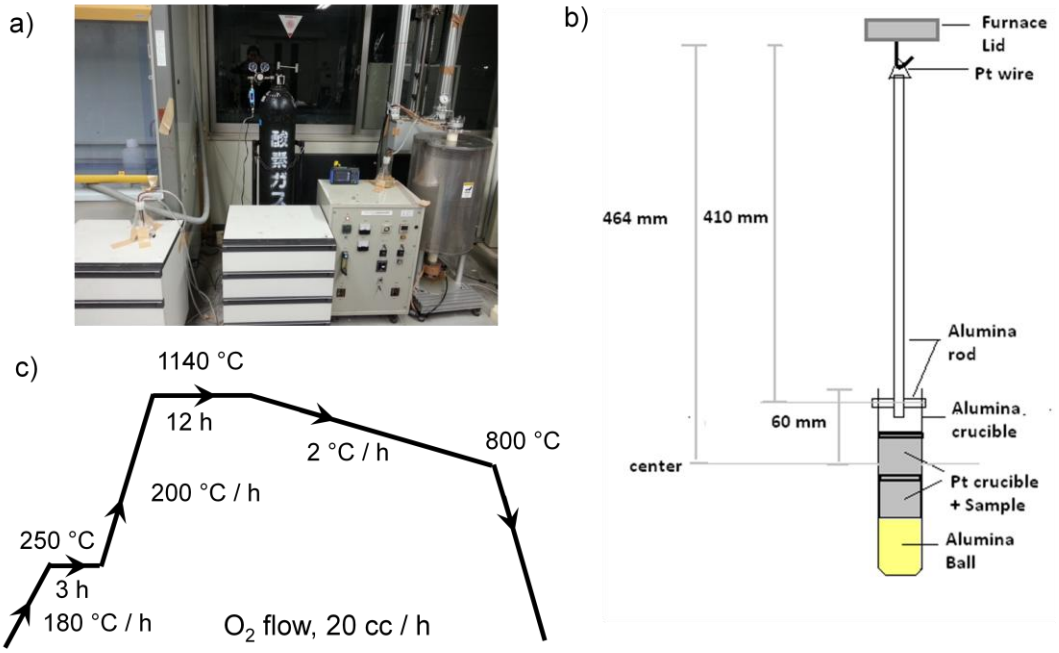

Figure 3.2 Experimental setup for the single crystal synthesis of $Ba_3CuSb_2O_9$: a) Bridgman furnace (right) at Material Synthesis Room, ISSP 5th Floor. b) Position of the sample inside the furnace. c) Temperature sequence used in the synthesis process.

3.2. Characterization

3.2.1. X-Ray Diffraction

X-ray diffraction is one of the primary characterization techniques for crystalline solid. This method is based on the diffraction phenomenon of X-ray wave by the atomic planes of the crystal. The X-ray can capture internal structure of a crystal because its wavelength ($\lambda \sim 1.547$ Å for Cu K alpha 1) is close to the interatomic distance in crystal ($\sim 10^{-10}$ m). The diffraction occurs only when incoming and diffracted wave vector satisfy Laue's equation,

$$\begin{aligned} \Delta\boldsymbol{k} &= \boldsymbol{k} - \boldsymbol{k}_0 = \boldsymbol{G} \\ \boldsymbol{a}\cdot\Delta\boldsymbol{k} &= 2\pi h \\ \boldsymbol{b}\cdot\Delta\boldsymbol{k} &= 2\pi k \\ \boldsymbol{c}\cdot\Delta\boldsymbol{k} &= 2\pi l \end{aligned} \tag{3.1}$$

with $\boldsymbol{k}$,$\boldsymbol{k}_0$, and $\Delta\boldsymbol{k}$ being diffracted beam wavevector, incoming beam wavevector, and scattering vector respectively. Here, $\boldsymbol{a}$, $\boldsymbol{b}$, and $\boldsymbol{c}$ are the crystal's primitive vector, and h, k, and l are the Miller indices of reciprocal lattice vector $\boldsymbol{G}$ ($\boldsymbol{G}$ = h$\boldsymbol{a}^*$ + k$\boldsymbol{b}^*$ + l$\boldsymbol{c}^*$). Thus, Laue equation can also be written as $\Delta\boldsymbol{k} = \boldsymbol{G}$**.** In case that $\boldsymbol{k} = \boldsymbol{k}_0$ (elastic scattering) and because $\boldsymbol{G} = -\boldsymbol{G}$, the Laue equation would be reduced to Bragg law

$$2d_{hkl}\sin\theta = n\lambda \tag{3.2}$$

The Bragg law is basically the diffraction condition for constructive interference, which can be realized if the all diffracted beam are in-phase. This law also indicates that every crystal plane has their own diffraction angle (i.e. diffraction occurs only for a specific incident angle and the beam will be diffracted to a specific diffraction angle).

Another important parameter in crystal diffraction is the structure factor. Structure factor relates the atomic arrangement in the lattice with the intensity of diffracted beam.

$$F_{hkl} = \sum_{i=1}^{N} f_i \exp\left[2\pi i\left(hu_i + kv_i + lw_i\right)\right] \tag{3.3}$$

with u_i, v_i, and w_i are the atomic coordinates of the i^{th} atom. Thus, the above equation will give condition of h, k, and l that would satisfy non-zero F_{hkl}.

There are mainly three components in X-ray diffraction: X-ray source, sample stage, and a scintillation detector. In a macroscopic level, the X-ray is generated by bombarding a target material (in our case Cu) with thermal electron which accelerated by a high voltage difference between the electrode. In atomic level, the X-ray radiation is generated by two mechanisms: Bremsstrahlung and characteristic radiation. Bremsstrahlung (meaning "braking radiation") is released as the high speed electron deflected by the nucleus. The Bremsstrahlung has continuous spectrum that depends on the incoming electrons' energy.

On the other hand, characteristic radiation is emitted as the electron in the target material as they move from outer shell to inner shell (energy level). Because the energy levels in atom are specific, the X-ray radiation also possesses a specific wavelength.

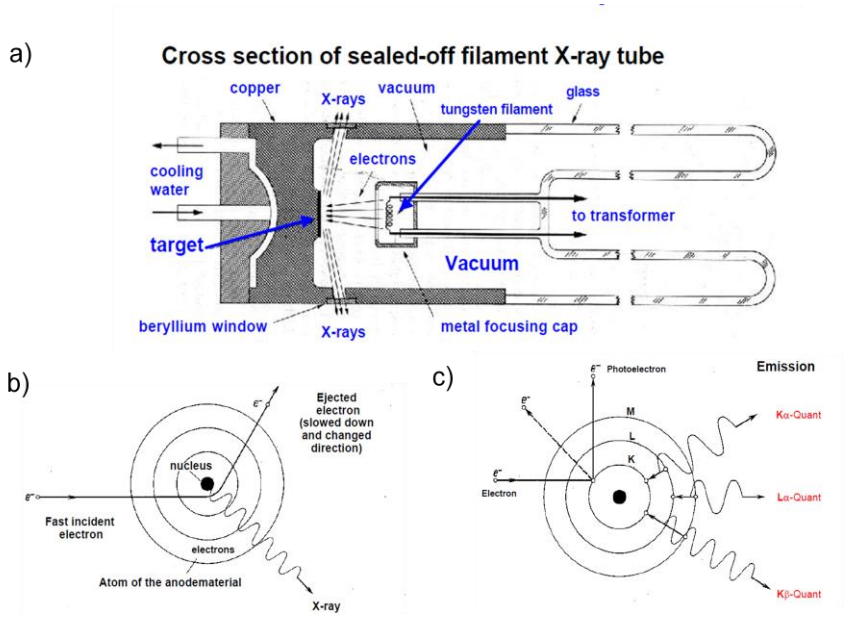

Figure 3.3 a) Cross section of X-ray tube[1]. The mechanism of X-ray generation: b) Bremsstrahlung and c) characteristic radiation[2].

Nowadays, the geometry that commonly used in powder diffraction measurement is Bragg-Brentano. In Bragg-Brentano type diffractometer, incident angle is taken as the angle between x-ray source and surface of the sample and diffracted angle calculated with respect to the incoming beam. Therefore, the diffraction vector is always perpendicular to the surface of sample. This can be achieved in two-ways: a) Sample stage is fixed, both X-ray source and detector are moving along measurement circle in the opposite direction (clockwise-counterclockwise) with the same speed of θ° /minute, or b) the X-ray source is now fixed, the sample is rotated with angular speed θ° /minute, and detector move along measurement circle in the same direction as the sample rotation, but with double angular speed (Figure 3.4b).

In this thesis, we used powder diffraction XRD to characterize our sample. Our X-ray diffractometer (Rigaku RINT2000) is Bragg-Brentano θ-2θ type with Cu as the target. The sample is prepared on top of a glass sample holder and ethanol is used to bind and distribute the powder on top of the sample holder's surface. Measurement at low temperature is performed using He cryostat installed in the same diffractometer.

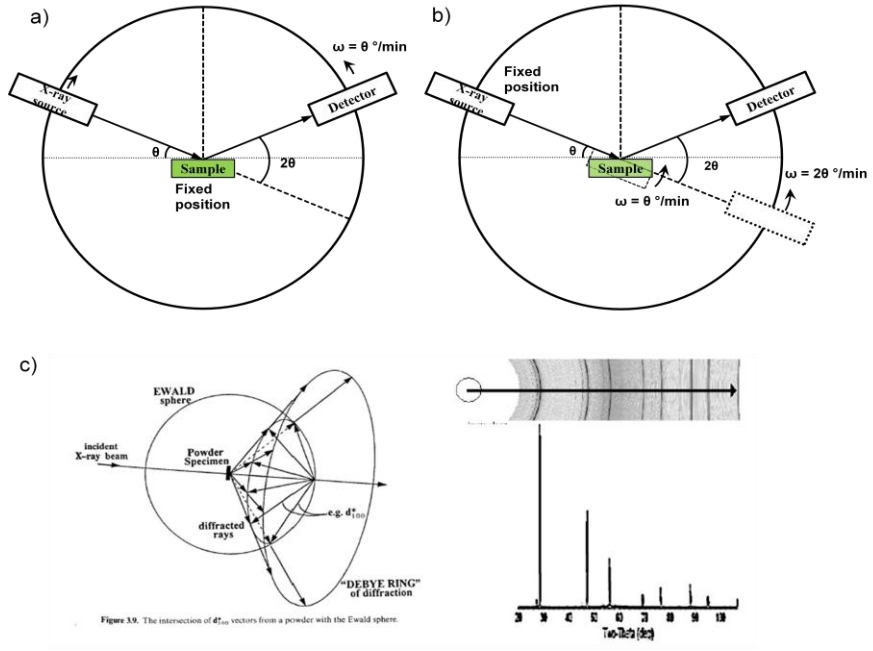

Figure 3.4 Two kinds of Bragg-Brentano geometry for X-ray diffraction measurement. a) *θ-θ* type with fixed sample and movable X-ray source and detector b) *θ-2θ* type fixed X-ray source and movable sample holder and detector. c) Debye ring of diffraction. A detector scans through an arc that cross each ring once, producing linear diffraction pattern [3].

3.2.2. Magnetization

Magnetic susceptibility is a quantity that relates magnetization ***M*** of a sample with the total external magnetic field ***H***

$$\boldsymbol{M} = \chi \boldsymbol{H} \tag{3.4}$$

In paramagnetic region, the susceptibility can be expressed as a function of temperature

$$\frac{\boldsymbol{M}}{\boldsymbol{H}} = \chi = \frac{\mu_0 N_A {\mu_{eff}}^2 {\mu_B}^2}{3k_B\left(T-\theta_{CW}\right)} = \frac{C}{T} \tag{3.5}$$

Here μ_0 is vacuum permeability constant, μ_B is Bohr magneton, μ_{eff} is effective moment, N_A is Avogadro's number, k_B is Boltzmann constant, T is temperature, C is Curie constant, and θ_{CW} is Curie-Weiss temperature. Effective moment then can be calculated when one plots the inverse susceptibility as a function of temperature

$$\frac{1}{\chi} = \frac{\left(T-\theta_{CW}\right)}{C} = \frac{3k_B}{\mu_0 N_A {\mu_{eff}}^2 {\mu_B}^2}\left(T-\theta_{CW}\right) \tag{3.6}$$

When a linear regression is performed on the inverse susceptibility versus temperature, the effective moment and Curie-Weiss temperature can be calculated as follows:

$$\frac{1}{\chi} = bT + a$$

$$b = \frac{1}{C}\ ;\ a = \frac{\theta_{CW}}{C} = b\theta_{CW};\ C = \frac{\mu_0 N_A \mu_{eff}{}^2 \mu_B{}^2}{3k_B} \tag{3.7}$$

$$\boxed{\mu_{eff}\mu_B = \sqrt{\frac{3k_B C}{\mu_0 N_A \mu_B}} \approx \sqrt{\frac{8}{b}}\ \mu_B}$$

$$\boxed{\theta_{CW} = \frac{a}{b}}$$

In this experiment, the magnetic susceptibility above 2 K is measured by using Superconducting Quantum Interference Device (SQUID) magnetometer installed in the commercial Magnetic Properties Measurement System (MPMS) made by Quantum Design. The low temperature AC and DC susceptibility (T < 1 K) is also measured by a homemade SQUID which is installed in a dilution refrigerator at ISSP, University of Tokyo.

A SQUID is basically a device which can be used as an ultra sensitive magnetometer (sensitivity up to 10^{-14} T) that operates based on Josephson Effect. DC SQUID utilizes two parallel Josephson junctions (superconductor - thin insulator - superconductor junction) (figure 3.5). A properties of Josephson junction is that the magnetic flux is quantized

$$\Phi_o = \frac{2\pi\hbar}{2e} = 2.0678\times10^{-15} Tesla.meter^2 \tag{3.8}$$

When a bias current is applied, it will be split equally across the two junctions. A change in the magnetic flux across the loop will generate induction current that tries to reduce magnetic flux (similar to Lenz's law). This induction current will flow in the opposite direction at one junction and the same direction at another junction. Due to the quantization of magnetic flux, the induction current will change direction for every ϕ /2 increase in magnetic flux. Once the current passes some threshold value, a voltage will appear across the junction. Thus, an increasing magnetic flux will be observed as oscillation in the SQUID voltage. The sample is prepared by mounting it on top of quartz rod by insulating varnish. The sample is then moved across the SQUID pick-up coil under a magnetic field in order to obtain magnetization.

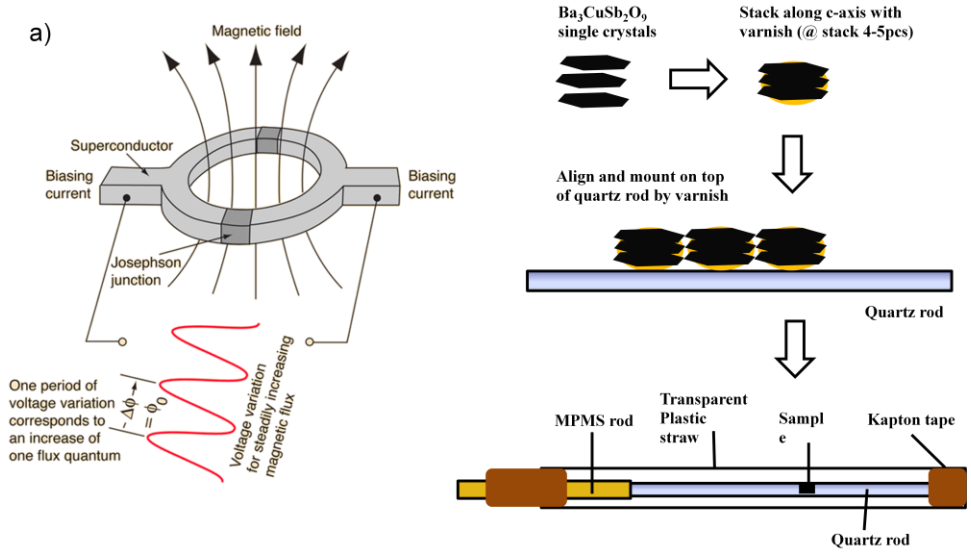

Figure 3.5 a) The principle of SQUID operation[4] b) Sample setup for magnetization measurement in MPMS.

3.2.3. Specific Heat

Specific heat is one of the useful thermodynamic quantities which relates the heat flow to the temperature change as in the following equation,

$$C = \frac{dQ}{dT} \tag{3.9}$$

Since heat transfer is a path-dependent process, one needs to choose in which process the heat is transferred. Two useful quantities are commonly used:

$$\begin{aligned} C_V &= \left(\frac{\partial U}{\partial T}\right)_V = \left(\frac{\partial Q}{\partial T}\right)_V \\ C_P &= \left(\frac{\partial H}{\partial T}\right)_P = \left(\frac{\partial Q}{\partial T}\right)_P \end{aligned} \tag{3.10}$$

In actual measurements, it is easier to keep pressure constant rather than volume constant. Therefore we usually obtain C_P that can be related to C_V by

$$C_P - C_V = \frac{\alpha^2}{\kappa} VT \tag{3.11}$$

here, α is the coefficient of thermal expansion and κ is the coefficient of isothermal compressibility. In a magnetic system at low temperatures, the specific heat can be expressed as a linear sum contributed by various degrees of freedom,

$$
\begin{aligned}
C_P &= C_{Phonon} + C_{Electron} + C_{Magnetic} + C_{Nuclear} + C_{Schottky} \\
C_{Phonon} &= AT^3 \\
C_{Electron} &= \gamma T \\
C_{Nuclear} &= \frac{A}{T^2} \\
C_{Schottky} &= \left(R \frac{\left(\frac{\Delta_B}{k_B T}\right)^2 \exp\left(\frac{\Delta_B}{k_B T}\right)}{\left(1+\exp\left(\frac{\Delta_B}{k_B T}\right)\right)^2} \right)
\end{aligned}
\tag{3.12}
$$

Another useful quantity is the entropy *S*. The difference in the entropy can be calculated from the specific heat

$$S = \int_{T_0}^{T} \frac{C}{T} dT \tag{3.13}$$

Specific heat can be measured in various ways. One way to measure the specific heat is by a relaxation method. In relaxation method, the total heat capacity is given by,

$$C = \kappa \cdot \tau \tag{3.14}$$

where κ is the thermal conductance between a sample platform and thermal bath, and τ is the relaxation time constant of a sample platform. At first the sample holder and sample are held in thermal equilibrium. The power of P_0 is applied to the sample holder, until thermal equilibrium is reached at $t = t_1$. Power is then switched off and the sample temperature relaxes towards thermal bath temperature according to

$$T_S - T_{Bath} = \Delta T \exp\left(-t/\tau\right) = P_0 \, \mathrm{R}_{Bath} \exp\left(-t/\left(C_S + C_{SH}\right) R_{Bath}\right) \tag{3.15}$$

The T_{bath} then changed and measurement is repeated to obtain a set of (C_{S}+C_{SH}) data as a function of temperature. At lower temperatures the thermal resistance between the sample and the sample holder R_{SH} cannot be neglected. The thermal relaxation then described with two time constants

$$
\begin{aligned}
T_S - T_{Bath} &= A_1 \exp\left(-t/\tau_1\right) + A_2 \exp\left(-t/\tau_2\right) \\
A_1 + A_2 &= \Delta T = P_0 R_{Bath}
\end{aligned}
\tag{3.16}
$$

Solving the equation (3.16), we obtain the total specific heat as

$$C_S + C_{SH} = K\left(\frac{A_1\tau_1 + A_2\tau_2}{A_1 + A_2}\right) \tag{3.17}$$

τ_2 may actually too small to be measured, so a better approximation would be [5]

$$C_S + C_{SH} \approx \frac{A_1 \tau_1}{\Delta T} R_{Bath} \tag{3.18}$$

In this experiment, we measure the heat capacity of $Ba_3CuSb_2O_9$ by the relaxation method using Physical Properties Measurement System (PPMS, Quantum Design) at Nakatsuji Laboratory, ISSP, University of Tokyo. In order to achieve low temperature region, we use a He3 system provided by Quantum Design. Before measuring the heat capacity of sample, we measure heat capacity of the sample holder with N-Apiezon grease attached to the sample platform. Then we perform the heat capacity measurements under several magnetic fields.

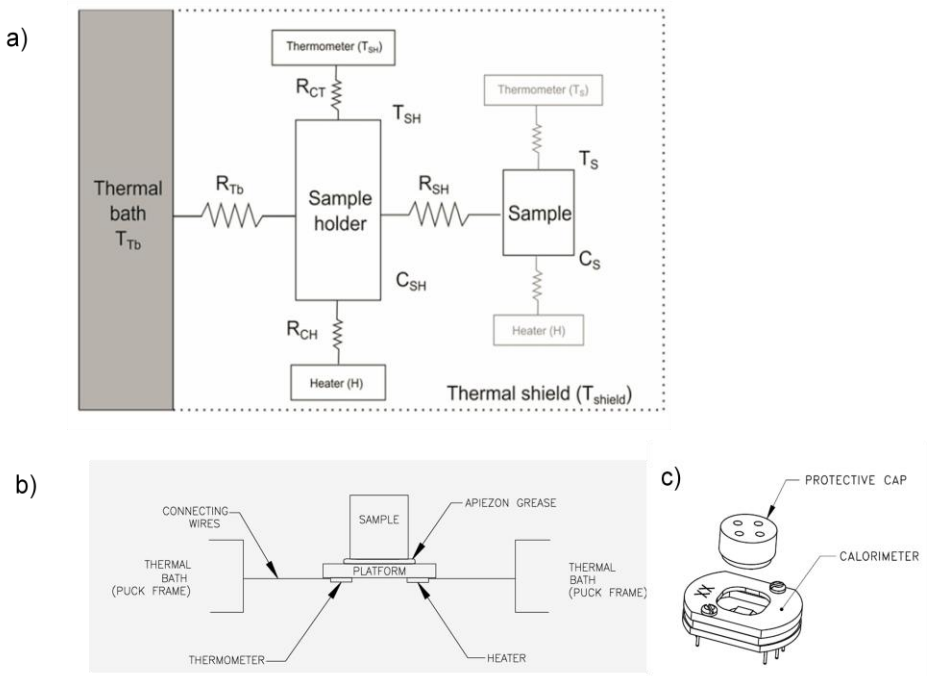

Figure 3.6 a) Scheme of calorimeter main elements[6]. b) Schematic picture of PPMS Heat Capacity Puck (Calorimeter). c) Puck for He3 System [7].

References:

1. http://web.pdx.edu/~pmoeck/phy381/Topic5a-XRD.pdf
2. http://www.smcr.fisica.unam.mx/8temasutiles/articulosutiles/Bas-XRD.pdf
3. http://prism.mit.edu/xray/oldsite/Basics%20of%20X- Ray%20Powder%20Diffraction.pdf
4. http://hyperphysics.phy-astr.gsu.edu/hbase/solids/squid.html
5. Shepherd, J.P. *Rev. Sci. Instrum.* **56**, 273-277 (1965)
6. G. Ventura, M. Perfetti, *Thermal Properties of Solids at Room and Cryogenic Temperatures.* p.39-67 *Springer* (2014)
7. PPMS Heat Capacity Option User's Manual, *Quantum Design*

Chapter 4

Results and Discussion

4.1. X-ray Diffraction

4.1.1. Polycrystalline sample

Polycrystalline samples of $Ba_3CuSb_2O_9$ are characterized by powder X-ray diffraction. The powder diffraction data of the several polycrystalline samples are shown in figure 4.1. Lattice parameters then calculated by performing *Whole Powder Pattern Fitting* procedure (Pawley method) on powder diffraction data.

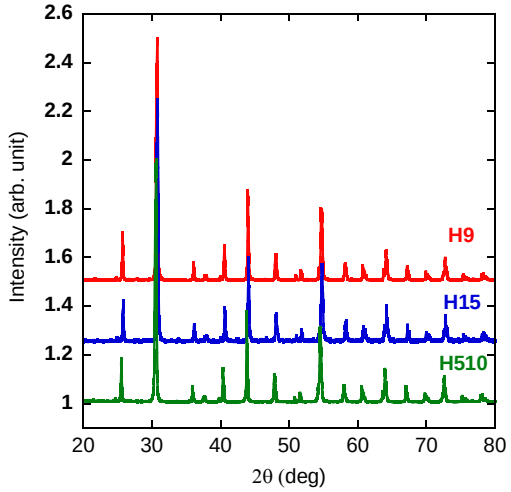

Figure 4.1 Powder XRD for several $Ba_3CuSb_2O_9$ polycrystalline samples

Sample #	Synthesis Method *	Lattice constant a ; c (Å)	Ba : Cu : Sb ratio
H9	Method 1	5.8054 ; 14.3249	3.01 : 1 : 2.06
H15	Method 2	5.8063 ; 14.3269	2.95 : 1 : 2.07
H510	Method 3	5.8091 ; 14.3343	3.09 : 1 : 2.09

*See figure 3.1 for details

Table 4.1 Lattice parameter and elemental composition for polycrystalline $Ba_3CuSb_2O_9$

Composition analysis has also been performed by Inductively Coupled Plasma - Atomic Emission Spectroscopy (ICP-AES). All samples are found to be single phase $Ba_3CuSb_2O_9$.

4.1.2. Single crystalline samples

The single crystalline samples of $Ba_3CuSb_2O_9$ are characterized by powder x-ray diffraction in both room and low temperature. Chemical analysis by ICP-AES is performed as well. As mentioned in previous section, there are two types of $Ba_3CuSb_2O_9$ single crystalline sample, *hexagonal* and *orthorhombic*. At room temperature, there is no difference of powder diffraction pattern. However, at low temperature, orthorhombic sample undergoes structural transition to orthorhombic structure (space group: *Cmcm*), indicated by the peak splitting. Visually, the hexagonal single crystal usually looks darker compared to orthorhombic sample, this might be related to the stoichiometry or valence of Cu. In terms of stoichiometry, the hexagonal sample usually has better Sb to Cu ratio than the orthorhombic sample.

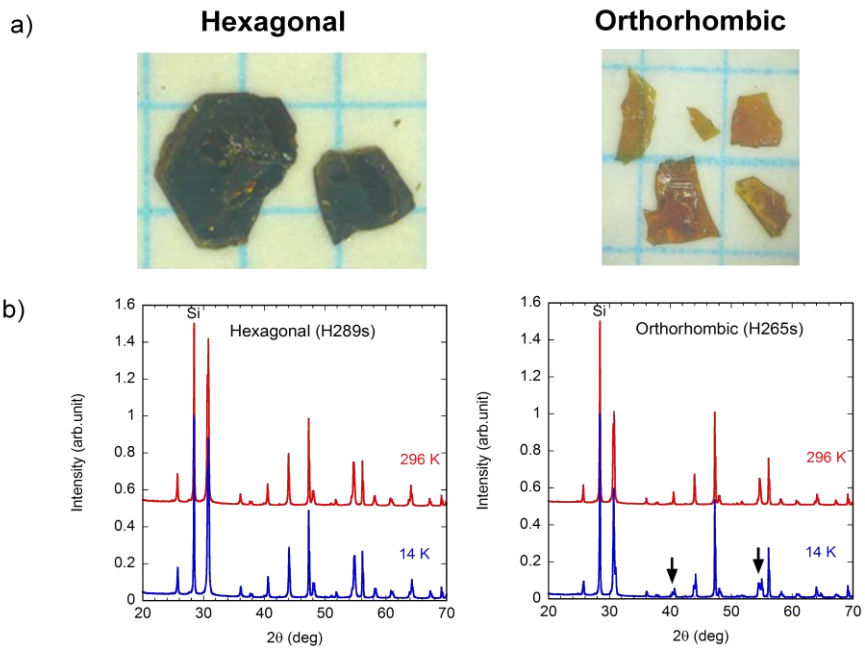

Figure 4.2 a) Hexagonal and orthorhombic sample of $Ba_3CuSb_2O_9$. b) Powder diffraction pattern at room and low temperature for hexagonal and orthorhombic sample. Arrows indicate associated peak splitting.

Sample #	Low Temp. Crystal structure	Room Temp. Lattice Constant *a* ; *c* (Å)	Ba : Cu : Sb ratio
H289s	Hexagonal	5.80286 ; 14.3263	2.80 : 1 : 1.85
H412s	Hexagonal	5.80436 ; 14.3306	2.88 : 1 : 2.46
H265s	Orthorhombic	5.80562 ; 14.3272	2.95 : 1 : 2.82
k05s	Orthorhombic	5.8027 ; 14.3211	2.99 : 1 : 2.13

Table 4.2 Lattice parameter and Elemental ratio (normalized with respect to Cu) of several $Ba_3CuSb_2O_9$ single crystalline samples.

4.2. Magnetic Susceptibility

4.2.1. DC Susceptibility

DC susceptibility measurements at temperature above 2 K are performed by MPMS (Quantum Design). For polycrystalline sample, we found no magnetic order down to 2 K. A log-log plot of magnetic susceptibility versus temperature indicates *power law* dependence (T^{α}, $\alpha \approx -0.9$) for both high and low temperature part. This power law behavior may indicate the random singlet state[1] (similar to long range RVB model), where each Cu spin form singlet pair in random manner. The anomaly observed around 50 K may be related to the singlet formation gap. On the other hand M (H) curve at T = 2 K show no sign of saturation for magnetic field up to 7 T, indicating unbroken singlet pairs.

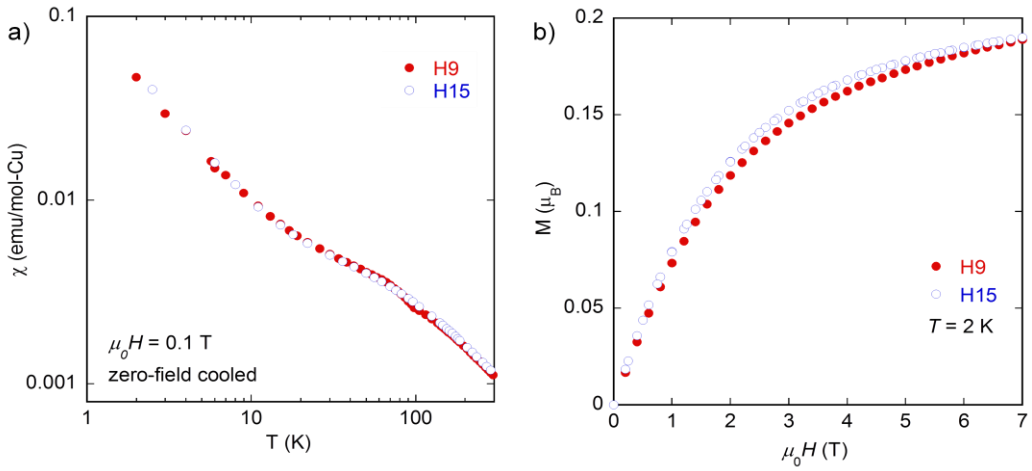

Figure 4.3 Magnetization of polycrystalline samples as function of a) temperature and b) applied magnetic field.

Sample #	μ_{eff}	θ_{CW}
H9	1.74	-40.89
H15	1.75	-38.32

Table 4.3 Effective moment and Curie-Weiss temperature of $Ba_3CuSb_2O_9$ polycrystalline samples.

DC susceptibility for single crystalline sample of $Ba_3CuSb_2O_9$ is measured by MPMS (for $T > 2$ K) and SQUID magnetometer at dilution refrigerator (for $T < 1$ K). The temperature dependence of magnetic susceptibility is similar to polycrystalline sample (no magnetic order, ~ $T^{-0.85}$ power law dependence at low temperature) (see also figure 4.6 b). Deviation from Curie-Weiss law (Curie tail) is found at the low

temperature part. This Curie tail is usually associated with the susceptibility contributed by the *orphan spin*[2]. Because singlet states carries no net spin, the magnetic susceptibility is expected to drop to zero when all spins form singlet state. However, the measured susceptibility show continuous increase below spin singlet formation temperature. Therefore, at low temperature, magnetic susceptibility is mainly contributed by the orphan spins. The total susceptibility then can be thought as a sum of bulk susceptibility and orphan spin susceptibility. A power law fit to low temperature data is used to extract bulk susceptibility. The bulk susceptibility indicates a clear peak at 50 K, which is close to the singlet formation temperature.

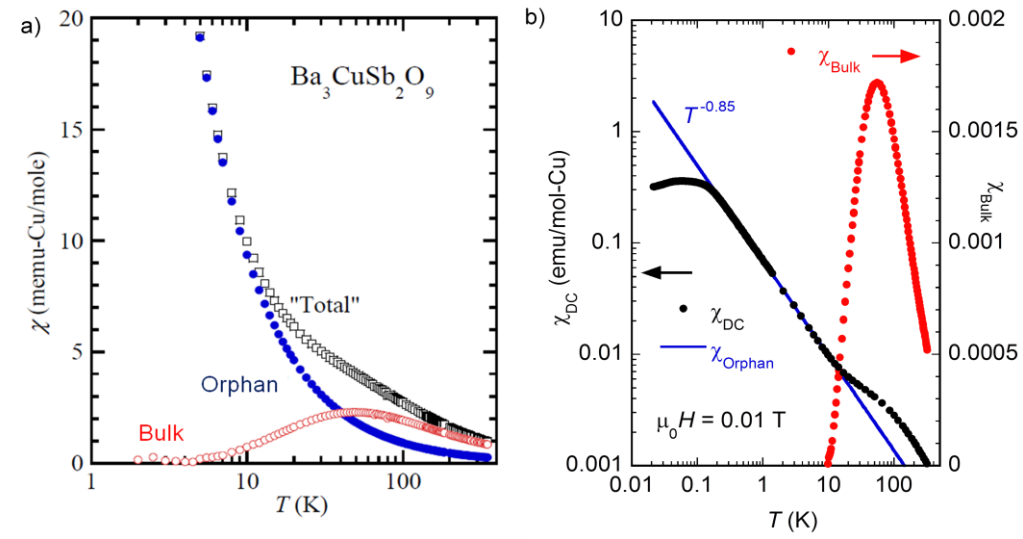

Figure 4.4 a) Total susceptibility as a sum of bulk and orphan spin susceptibility [3]. b) Extraction of bulk susceptibility by power law fit. A peak is found at 50 K, which may relate to the spin singlet formation.

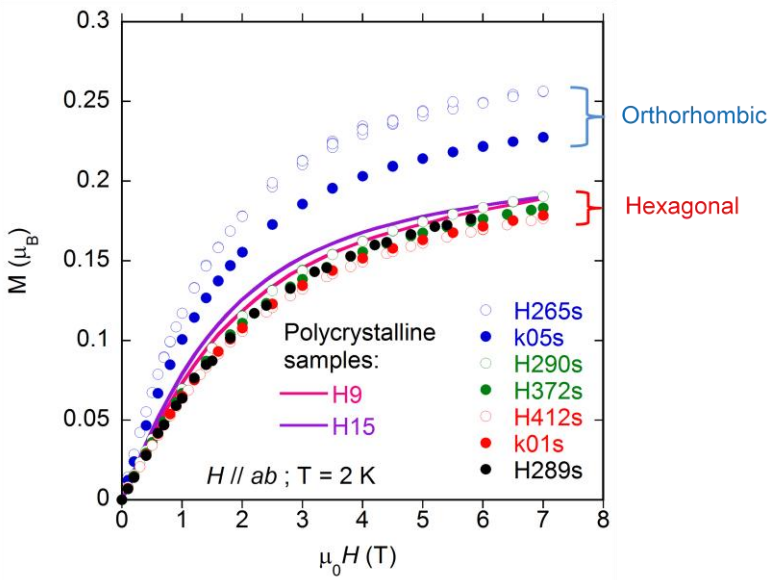

Figure 4.5 Magnetization versus magnetic field for several $Ba_3CuSb_2O_9$ single crystalline samples. *M (H)* curve for polycrystalline sample are put for comparison.

Interestingly, *M (H)* curve along *ab*-plane indicates systematic difference between the hexagonal and orthorhombic sample. The orthorhombic sample tends to have larger magnetization response to applied magnetic field. This might be due to larger amount of unpaired Cu spins (orphan spins) in orthorhombic sample.

A modified Brillouin function fitting on *M*(*H*) curve can be used to estimate the amount of orphan spin

$$M(H) = f_{orp} \times gS\mu_B \tanh\left[\frac{g\mu_B H}{k_B(T-T_0)}\right] + \chi_{con} H \qquad (4.1)$$

f_{orp} is the amount of orphan spin in the sample and χ_{con} is the constant term of magnetic susceptibility. The f_{orp} estimated by this method varies between 12% for hexagonal sample and 18% for orthorhombic sample. The best hexagonal sample (k01s) coincidentally has the lowest saturated moment at higher field. So, *M* (*H*) measurement might be useful to estimate quality, particularly stoichiometry of $Ba_3CuSb_2O_9$ single crystals.

The low temperature DC and AC susceptibility measurement was performed on one of the hexagonal samples (H289s). In DC susceptibility, we found a broad peak around 120 mK, which is associated with the spin freezing. A hysteresis between zero-field cooled and field-cooled data as well as the peak suppression under small increase of magnetic field indicates the glassy properties of this spin freezing. The continuous rise of FC curve below T_f indicates that this system is different from homogeneous spin glass.

On the high temperature side of low temperature data (T ~ 2 K), the susceptibility data overlap pretty well with the polycrystalline samples. This indicates that the sample used in the measurement is stoichiometric hexagonal single crystals.

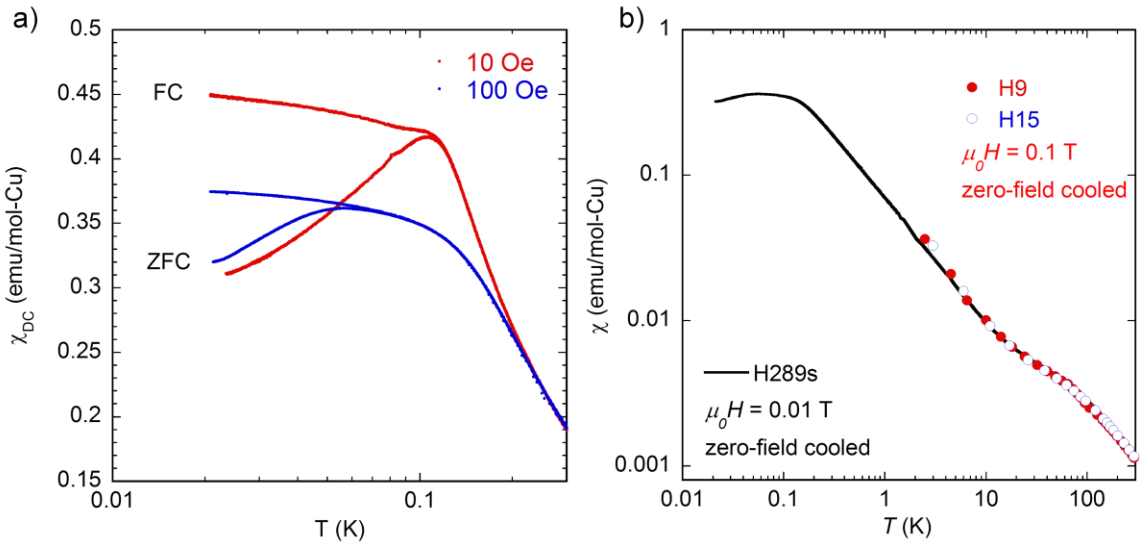

Figure 4.6 a) Low temperature DC susceptibility of hexagonal sample (H289s). b) Comparison with polycrystalline samples' magnetization.

The orphan spin fraction can also be estimated from Curie Weiss fit at low temperature by comparing the effective moment obtained at low temperature (T < 2 K) and high temperature (T > 50 K).

$$\frac{N_{LT}}{N_{HT}} \cong \left(\frac{\mu_{eff,LT}}{\mu_{eff,HT}} \right)^2 \tag{4.2}$$

From the equation (4.2), orphan spin fraction is estimated to be 12% of total spin, which is close to the result obtained by M (H) curve fitting.

Temperature	$\mu_{\mathbf{eff}}$ **(μB)**	$\theta_{\mathbf{CW}}$ **(K)**
0.2 K < T < 2 K	0.72	-0.06
50 K < T < 300 K	2.04	-65.7

Table 4.4 Effective moment and Curie-Weiss temperature obtained from low temperature and high temperature Curie-Weiss fit.

4.2.2. AC Susceptibility

In AC susceptibility, we found a slight frequency dependence of freezing temperature. However, the associated shift in freezing temperature is very small (in order of 1 - 2 mK), and so, lies within the error bar of freezing temperature determination. Nevertheless, we tried to investigate this frequency dependence further, in order to confirm glassy behavior observed in the DC susceptibility.

Frequency (Hz)	$T_{\mathbf{f}}$ **(K)**
1	0.118
10	0.120
100	0.122
1000	0.124

Table 4.5 T_f at various AC frequencies, as determined by linear extrapolation of the data near the susceptibility peak.

There are several theories that can be use to explain relaxation kinetics (i.e. temperature dependence of characteristic relaxation time). The first one is Arrhenius law,

$$f = f_0 \exp\left(-\frac{E_A}{k_B T_f} \right) \tag{4.3}$$

Here, T_f is freezing temperature, E_A is the activation energy, k_B is the Boltzmann constant, and f_0 is the characteristic frequency. Arrhenius law initially used to describe kinetic of chemical reaction, however it

can also be used to describe relaxation kinetics that involve energy barrier between initial and final states (activation type transition).

Another useful relation is the Vogel-Fulcher-Tammann (VFT) law which describes relaxation kinetics for spin glass, particularly the one which has cooperative behavior (interacting particles).

$$f = f_0 \exp\left(-\frac{E_A}{k_B\left(T_f - T_0\right)}\right) \tag{4.4}$$

Yet another useful empirical relation between freezing temperature and frequency

$$g = \frac{\Delta T_f}{T_f \Delta \log f} \tag{4.5}$$

where the value of g is between 0.005 - 0.028 for canonical spin glass. For $Ba_3CuSb_2O_9$ the g value is 0.0167, which is close to the value expected for spin glass.

Both VFT and Arrhenius law, however, fail to describe relaxation kinetic of $Ba_3CuSb_2O_9$ at low temperature (typical value of τ_0 for spin glass is about 10^{-11} s). Rearranging Arrhenius equation, the following relation is obtained

$$\ln f = \ln f_0 - \frac{E_A}{k_B}\frac{1}{T} \tag{4.6}$$

Therefore, E_A / k_B and f_0 can be calculated from the slope of linear fit of ln f against 1/ T. Similarly, the VFT equation can also be rearranged as

$$\ln f = \ln f_0 - \frac{E_A}{k_B}\frac{1}{T - T_0} \tag{4.7}$$

, and using the above equation to fit ln f versus T curve would give E_A / k_B, T_0 and f_0.

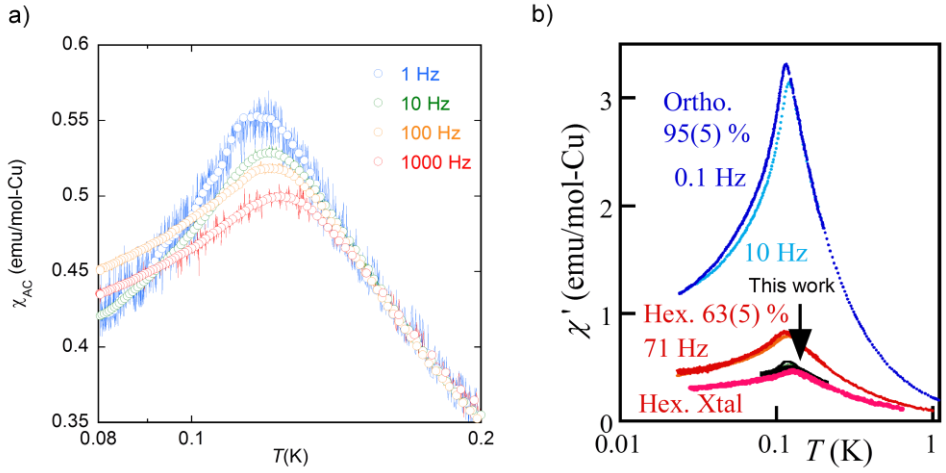

Figure 4.7 a) AC susceptibility vs. temperature (Open circles: smoothed data). b) This work's result compared to previous report on polycrystalline sample[3].

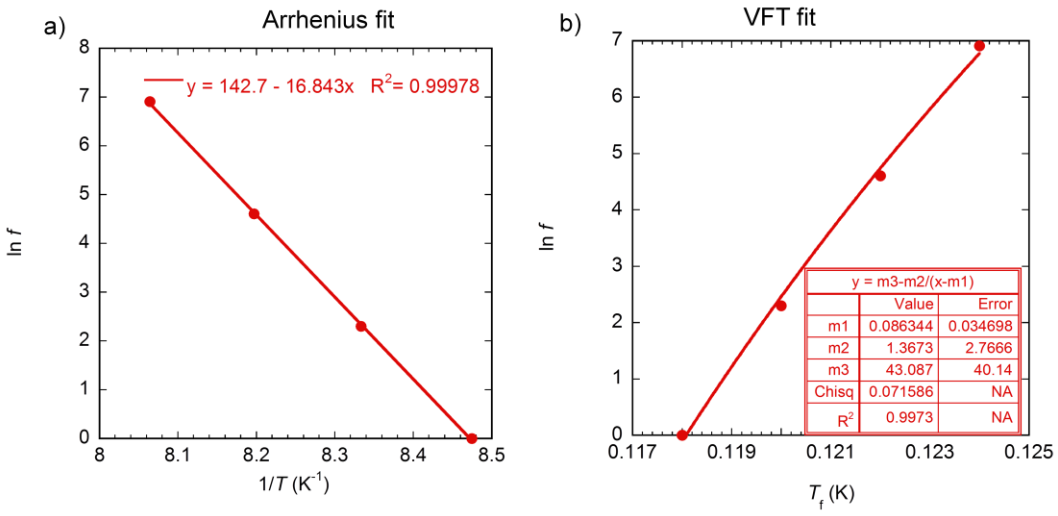

Figure 4.8 a) Arrhenius fit and b) VFT fit to the *ln f* as function of T_f

Method	E_A / k_B	τ_0	T_0 **(K)**
Arrhenius	16.8 K	1.06 x 10^{-62} s (unphysical)	-
VFT	1.3 K	1.9 x 10^{-19} s (too small)	0.086

Table 4.6 Fit result of T_f as function of frequency

4.3. Specific Heat

The specific heat of hexagonal sample (k01s) of $Ba_3CuSb_2O_9$ at low temperature is measured by PPMS Quantum Design He3 system in Nakatsuji laboratory, ISSP, University of Tokyo. The magnetic part of specific heat is obtained by subtracting total specific heat with the specific heat of non-magnetic analog compound $Ba_3ZnSb_2O_9$.

The low temperature part of magnetic specific heat is dominated by the Schottky-like specific heat which may originate from orphan spin contribution. The Schottky anomaly is gradually suppressed as applied magnetic field increases, but remains visible under magnetic field up to 9 T. At low temperature end of magnetic specific heat, a linear behavior can be observed for C_M under $B > 5$ T, consistent with the previous study[4]

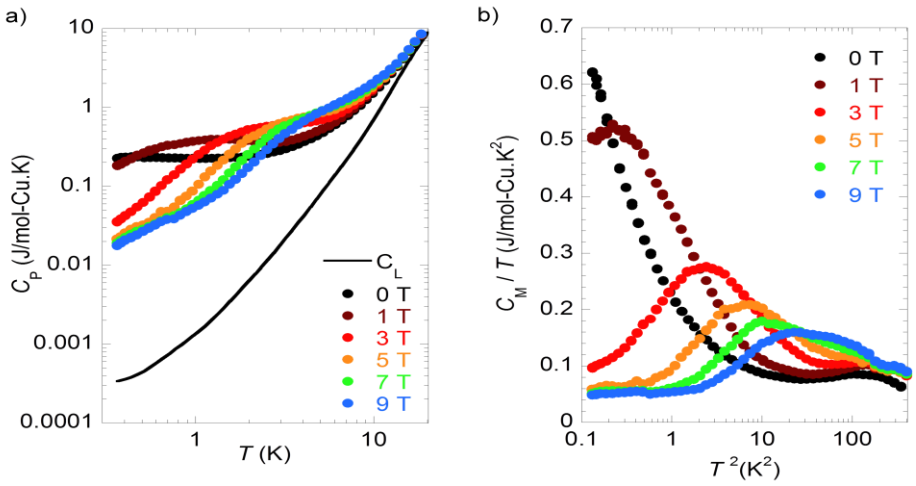

Figure 4.9 a) Total specific heat as function of temperature. b) C_M / T versus T^2 at various magnetic fields.

The Schottky specific heat is estimated by fitting the total specific heat with the following equation

$$C_P = C_{other} + C_{Schottky}$$
$$= \left(AT^3 + BT + \frac{C}{T^2} \right) + \left(R \times f_{orphan} \times \frac{\left(\frac{\Delta_B}{k_B T} \right)^2 \exp\left(\frac{\Delta_B}{k_B T} \right)}{\left(1 + \exp\left(\frac{\Delta_B}{k_B T} \right) \right)^2} \right) \quad (4.8)$$

here f_{orp} is the orphan spin fraction, and the Schottky anomaly is assumed to come from two-energy-level model which is separated by a gap Δ_B. The fitting result is summarized in table 4.7. The obtained parameters are then further refined by linear fit to obtain f_{orp} (lin) and Δ_B / k_B (lin). These parameters are used to estimate Schottky specific heat at each magnetic field. The bulk susceptibility is then calculated by subtracting magnetic specific heat with the Schottky specific heat. The result is shown in figure 4.10.

B (T)	f_{orp}	Δ_B / k_B (K)	f_{orp} (lin)	Δ_B / k_B (lin) (K)
0	0.03979	2.2082	0.058860	1.0201
1	0.08466	2.5687	0.066504	2.4954
3	0.12804	5.5364	0.081791	5.4460
5	0.10407	8.1659	0.097079	8.3966
7	0.11165	11.237	0.11237	11.347
9	0.12231	14.472	0.12765	14.298

Table 4.7 Curve fitting result and estimated f_{orp} and Δ_B / k_B from linear fit.

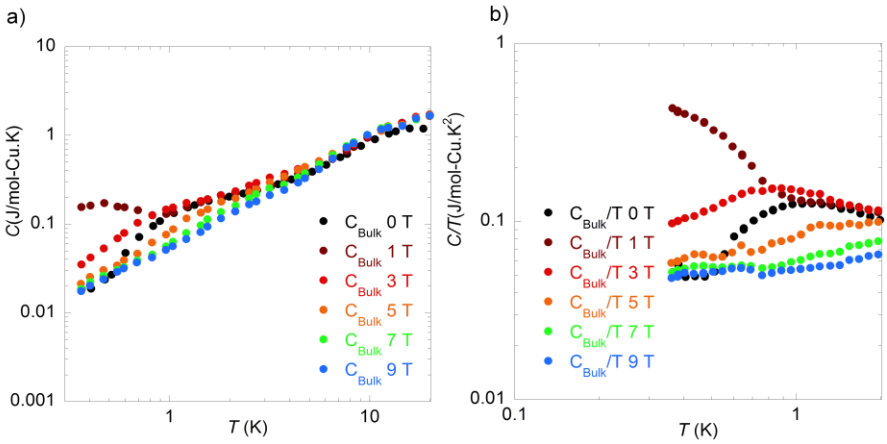

Figure 4.10 a) Bulk specific heat as function of temperature. b) C_{Bulk}/T versus T plot.

It can be seen that for low magnetic field data, our model is inadequate to completely remove Schottky specific heat. Indeed, by arbitrarily choosing *two* sets of f_{orp} and Δ_B / k_B, the lower magnetic field specific heat data will overlap to the high field specific heat. The situation is characteristic of *Random Singlet State* and recent NMR result suggested a crossover to multiple gapped ground states[5]. The linear temperature dependence is one of the characteristic properties of gapless quantum spin liquid. In $Ba_3CuSb_2O_9$, the linear temperature dependence can also be seen *for* high magnetic field data. A linear extrapolation to the *y*-axis give the γ value, which is about 50 mJ/mol.K for $Ba_3CuSb_2O_9$ .This value is close to the γ value for quantum spin liquid, which ranged from 1-250 mJ/mol.K.

It would be interesting to calculate Wilson ratio of $Ba_3CuSb_2O_9$. From Curie-Weiss fit at low temperature side of DC susceptibility, one can obtain χ_0, which is about 9.3 x 10^{-4} emu/mol. The Wilson ratio, defined as,

$$R \equiv \frac{4}{3}\left(\frac{k_B \pi}{g \mu_B}\right)^2 \frac{\chi_0}{\gamma} \tag{4.9}$$

should be in order of unity in case the spin-orbit coupling is absent. In $Ba_3CuSb_2O_9$, the Wilson ratio is approximately 1.07. This value indicates that spin-orbit coupling is absent and thus has no contribution to the magnetic susceptibility at low temperature.

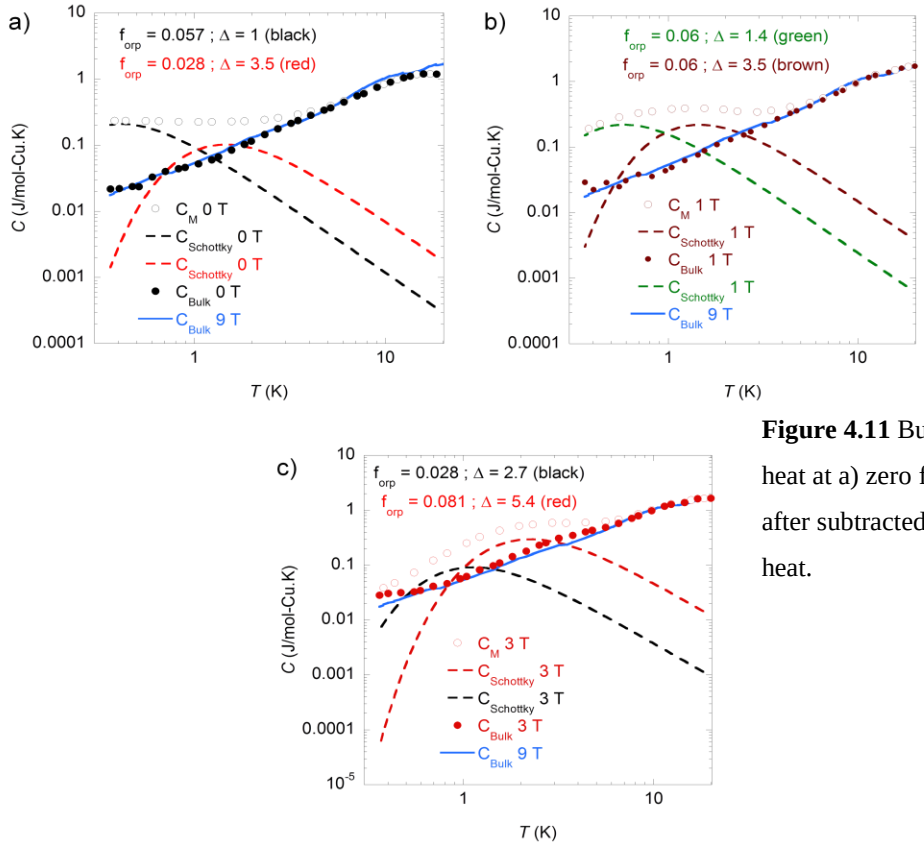

Figure 4.11 Bulk susceptibility of specific heat at a) zero field, b) 1 T, and c) 3 T, after subtracted with two Schottky specific heat.

.

References:

1. D. S. Fisher, *Phys. Rev. B* **50**, 6 (1994)
2. P. Schiffer and I. Daruka , *Phys. Rev. B* **56**, 21 (1997)
3. S. Nakatsuji et al., *Science* **336**, 559-563 (2012)
4. H. D. Zhou et al., *Phys. Rev. Lett.* **106**, 147204 (2011)
5. Quilliam et al. arXiv:1207.6469 [cond-mat.str-el]

Chapter 5
Conclusion

In this thesis, I have performed

- Synthesis of $Ba_3CuSb_2O_9$ single crystalline and polycrystalline sample
- Characterization of $Ba_3CuSb_2O_9$:
  a. Magnetic properties of polycrystalline and single crystalline sample at low temperature
  b. Specific heat of single crystalline sample at low temperature

and found

- Spin freezing at 120 mK, which is glassy in nature, indicated by hysteresis between ZFC-FC DC Susceptibility, and slight frequency dependence of freezing temperature in AC susceptibility
- Power-law behavior in temperature dependence of magnetic susceptibility, possibly contributed by the orphan spins.
- Relaxation kinetics at low temperature cannot be described in terms of simple spin glass
- Linear temperature dependence of bulk specific heat, which become more obvious in high magnetic field. The Schottky specific heat is contributed by orphan spin which can be removed completely by using at least two Schottky heat capacity with different orphan spin fraction and energy gap.
- The physical parameter, such as Sommerfeld constant γ and Wilson ratio of $Ba_3CuSb_2O_9$ is close to the value of many Quantum Spin Liquid candidates.